



Article

The Potential of Using SDGSAT-1 TIS Data to Identify Industrial Heat Sources in the Beijing–Tianjin–Hebei Region

Yanmei Xie ^{1,2,*}, Caihong Ma ^{1,2,*} , Yindi Zhao ¹ , Dongmei Yan ^{1,2,3}, Bo Cheng ², Xiaolin Hou ^{1,2}, Hongyu Chen ⁴, Bihong Fu ⁵ and Guangtong Wan ^{1,2}

- ¹ College of Environment and Spatial Informatics, China University of Mining and Technology, Xuzhou 221116, China; xieyanm@cumt.edu.cn (Y.X.); zhaoyd@cumt.edu.cn (Y.Z.); yandm@aircas.ac.cn (D.Y.); ts22160114p31@cumt.edu.cn (X.H.); wangt@aircas.ac.cn (G.W.)
- ² Aerospace Information Research Institute, Chinese Academy of Sciences, Beijing 100094, China; chengbo@aircas.ac.cn
- ³ University of Chinese Academy of Sciences, Beijing 100049, China
- ⁴ Institute of Optoelectronics, Fudan University, Shanghai 200433, China; chy_ioe@fudan.edu.cn
- ⁵ Innovation Academy for Microsatellites, Chinese Academy of Sciences, Shanghai 201204, China; fubh@microsat.com
- * Correspondence: mach@aircas.ac.cn; Tel.: +86-152-1067-5780

Abstract: It is crucial to detect and classify industrial heat sources for sustainable industrial development. Sustainable Development Science Satellite 1 (SDGSAT-1) thermal infrared spectrometer (TIS) data were first introduced for detecting industrial heat source production areas to address the difficulty in identifying factories with low combustion temperatures and small scales. In this study, a new industrial heat source identification and classification model using SDGSAT-1 TIS and Landsat 8/9 Operational Land Imager (OLI) data was proposed to improve the accuracy and granularity of industrial heat source recognition. First, multiple features (thermal and optical features) were extracted using SDGSAT-1 TIS and Landsat 8/9 OLI data. Second, an industrial heat source identification model based on a support vector machine (SVM) and multiple features was constructed. Then, industrial heat sources were generated and verified based on the topological correlation between the identification results of the production areas and Google Earth images. Finally, the industrial heat sources were classified into six categories based on point-of-interest (POI) data. The new model was applied to the Beijing–Tianjin–Hebei (BTH) region of China. The results showed the following: (1) Multiple features enhance the differentiation and identification accuracy between industrial heat source production areas and the background. (2) Compared to active-fire-point (ACF) data (375 m) and Landsat 8/9 thermal infrared sensor (TIRS) data (100 m), nighttime SDGSAT-1 TIS data (30 m) facilitate the more accurate detection of industrial heat source production areas. (3) Greater than 2~6 times more industrial heat sources were detected in the BTH region using our model than were reported by Ma and Liu. Some industrial heat sources with low heat emissions and small areas (53 thermal power plants) were detected for the first time using TIS data. (4) The production areas of cement plants exhibited the highest brightness temperatures, reaching 301.78 K, while thermal power plants exhibited the lowest brightness temperatures, averaging 277.31 K. The production areas and operational statuses of factories could be more accurately identified and monitored with the proposed approach than with previous methods. A new way to estimate the thermal and air pollution emissions of industrial enterprises is presented.

Keywords: industrial heat sources; production area; multiple features; SDGSAT-1 TIS; Beijing–Tianjin–Hebei



Citation: Xie, Y.; Ma, C.; Zhao, Y.; Yan, D.; Cheng, B.; Hou, X.; Chen, H.; Fu, B.; Wan, G. The Potential of Using SDGSAT-1 TIS Data to Identify Industrial Heat Sources in the Beijing–Tianjin–Hebei Region. *Remote Sens.* **2024**, *16*, 768. <https://doi.org/10.3390/rs16050768>

Academic Editors: Gilles Boulet, Mengmeng Wang, Vicente Burchard-Levine, Tian Hu and Jean-Louis Roujean

Received: 2 December 2023

Revised: 16 February 2024

Accepted: 21 February 2024

Published: 22 February 2024



Copyright: © 2024 by the authors. Licensee MDPI, Basel, Switzerland. This article is an open access article distributed under the terms and conditions of the Creative Commons Attribution (CC BY) license (<https://creativecommons.org/licenses/by/4.0/>).

1. Introduction

Industrial heat source production areas are areas where waste heat is generated and emitted as a result of the operation of industrial heat sources, such as the smelting and

rolling of nonferrous metals, cement production, oil refining, oil exploration, and chemical processing [1,2]. The development of industrial heat sources, requiring vast amounts of basic materials and equipment, is a significant driving force for national development. However, the large amount of industrial heat source emissions can significantly exacerbate air pollution [3–5]. Direct industrial emissions account for 21% of the global carbon dioxide emissions related to fossil fuels, with the steel industry being the highest emitter, contributing 5% of fossil fuel-related greenhouse gas emissions [6]. Moreover, anthropogenic CO₂ emissions from cement production constitute ~8% of global CO₂ emissions [7,8]. This not only impacts human health and quality of life but also causes long-term damage to the natural environment [9,10]. Therefore, establishing a comprehensive, accurate, and detailed inventory of industrial heat sources can aid in assessing air pollution, supporting environmental monitoring, analyzing energy consumption, assisting in industrial decision making, and implementing reform measures.

The complex spatial distribution and large number of industrial heat sources necessitate the use of remote sensing methods as alternatives to traditional approaches for obtaining relatively accurate information [11,12]. Currently, satellite remote sensing monitoring is being applied in various fields, such as tracking the expansion of urban construction [13], changes in forest cover [14], radiant emissions from urban nighttime lighting [15], and heat release activities in industrial areas [16]. Thermal infrared sensors can capture radiation energy differences caused by temperature variations, making them suitable for monitoring thermal emissions produced by industrial heat source production activities [17,18]. Several thermal infrared sensors, such as the Advanced Very High Resolution Radiometer (AVHRR), the Along Track Scanning Radiometer (ATSR) and Advanced ASTR (AATSR), the Visible and Infrared Scanner (VIRS), the Moderate Resolution Imaging Spectrometer (MODIS), the Visible Infrared Imaging Radiometer Suite (VIIRS), the Landsat 8/9 Thermal Infrared Sensor (TIRS), and the Sentinel-3 Sea and Land Surface Temperature Radiometer (SLSTR) [19–22], are available for generating heat-related products. These products are mostly used for identifying heat sources such as wildfires, agricultural burning, and volcanoes [23–26]. Only a few of these products are used for the identification and monitoring of industrial heat sources. In most of the existing related research, high-resolution optical remote sensing imagery [27,28] and thermal anomaly products were used for detecting and monitoring industrial heat source variations in large-scale areas [29–31]. Guo et al. [27] and Chen et al. [28] employed remote sensing imagery to explore the industrial layout of steel mills and the production equipment used. However, it remains challenging to determine whether a factory is in operation, and it is even more difficult to estimate heat emissions during the production process. Accurate industrial heat source detection using thermal infrared remote sensing data provides an objective and suitable way to identify and monitor industrial heat sources at a large scale [32–34]. Therefore, an increasing number of scholars have used thermal infrared remote sensing data or thermal anomalies to detect heat emissions from factories. Baugh used NPP VIIRS nighttime thermal anomaly data to detect the temporal and spatial distributions of natural gas flaring from 2012 to 2015 [35]. Elvidge et al. used the VIIRS Nightfire (VNF, 750 m) product to obtain the spatial locations of global natural gas flaring and found that the majority of natural gas flaring occurs primarily in upstream production areas [36]. Tkachenko et al. used Sentinel 2 data, acquired global cement plant locations, and described the characteristics of the cement production assets and their upstream suppliers [37]. However, their focus was predominantly on detecting specific types of factories or burning areas, and they did not monitor other categories of industrial heat sources. Liu first adopted the VIIRS VNF, combined with spatiotemporal temperature information, for the identification and classification of multiple classes of industrial heat sources [29]. Later, Ma introduced high-spatial-resolution VIIRS active-fire-point (ACF) data (375 m) and employed an enhanced adaptive K-means algorithm to detect industrial heat sources in small areas [30]. However, the temperature range of the VIIRS VNF product used by Liu for detecting thermal anomalies in industrial heat sources was 500–2500 K, and confidence in detection at temperatures below 500 K was

relatively low [29]. In addition, the VIIRS ACF product used by Ma can be used to detect the temperature of thermal anomalies ranging from 400 to 1200 K [38]. When the VNF or ACF product is used, smaller or cooler industrial heat sources might be overlooked. Using Landsat 8 thermal infrared sensor (TIRS) data and GF-2 image data, Zhou calculated the temperature difference between the main production areas and other regions to assess the economic activities of steel mills [39]. Han expanded upon Zhou's work and studied the seasonal, long-term production status of steel mills [34]. However, they studied only the production activities of factories and did not provide a method for detecting factories. Kato et al. used Landsat 8 OLI and Sentinel-2 MSI data to detect and classify global heat sources, from which numerous plants as small as a few square meters were obtained. The aforementioned studies were able to detect only the general locations of factories and could not identify the locations of the production areas within these factories. Therefore, a detection method that can be used to precisely identify industrial heat sources and production areas at lower temperatures and smaller scales is needed.

The launch of the Sustainable Development Science Satellite 1 (SDGSAT-1) offered a new approach for identifying industrial heat sources. Among the thermal infrared data types, SDGSAT-1 thermal infrared spectrometer (TIS) data exhibit the highest spatial resolution in civilian use and have been widely applied in tasks such as target detection and monitoring [40–42]. Therefore, in this study, SDGSAT-1 TIS data were first introduced to identify industrial heat sources and production areas, aiming to address the issues of the insufficient spatial precision in identifying industrial heat sources and the insensitivity to low-heat emission sources. The identification of new industrial heat source production areas and an industrial heat source classification model using SDGSAT-1 TIS and Landsat 8/9 Operational Land Imager (OLI) data were proposed. First, multiple features (combining thermal and optical features) were extracted using SDGSAT-1 TIS and Landsat 8/9 OLI data. Second, an industrial heat source production area identification model based on a support vector machine (SVM) and multiple features was constructed. Then, industrial heat source objects were generated and verified based on the topological correlation between the industrial heat source production area identification results and Google Earth images. Finally, the industrial heat source objects were classified into six categories based on point-of-interest (POI) data and high-resolution image data. The new model was applied to the Beijing–Tianjin–Hebei (BTH) region in China. The results showed that our new model could be employed to accurately identify industrial heat sources and production areas. This study supports a new way to effectively monitor and evaluate the operational statuses and heat emissions of industrial heat sources at a large scale. This approach can be used to estimate the heat emissions of industrial heat sources and it provides support for the industry to adjust its factory production and operation strategies and plans in a timely manner.

Descriptions of the study area, data sources, and methods used in this paper are provided in Section 2. The categorical characteristics and spatial distributions of the industrial heat sources identified by our new method are described in the Results Section. Third, an error analysis and comparative evaluation of industrial heat source production areas detected from three thermal infrared datasets and existing industrial heat source data are performed, and the significance and limitations of the study are discussed. Finally, the main conclusions are drawn in the last Section.

2. Materials and Methods

2.1. Study Area

The BTH region mainly comprises 13 cities and 200 districts and counties in the Beijing, Tianjin, and Hebei provinces (as shown in Figure 1). Located in the northern part of the North China Plain, the BTH region extends from 113°27'E to 119°50'E longitude and from 36°05'N to 42°40'N latitude. The region has a total population of 141.26 million people (2021) and a total area of approximately 217,200 km². As of 2020, Beijing encompasses 16 municipal districts, while Tianjin also comprises 16 municipal districts. The administrative division of Hebei Province is complex, consisting of 47 municipal districts,

27 county-level cities, and 94 counties. In the BTH region, Beijing serves as the core city, with Tianjin, Shijiazhuang, Tangshan, Baoding, and Handan functioning as regional central cities. Langfang, Cangzhou, Hengshui, Xingtai, Qinhuangdao, Zhangjiakou, and Chengde function as nodal cities, forming a regional development pattern characterized by one core, two cities, three axes, four areas, and multiple nodes.

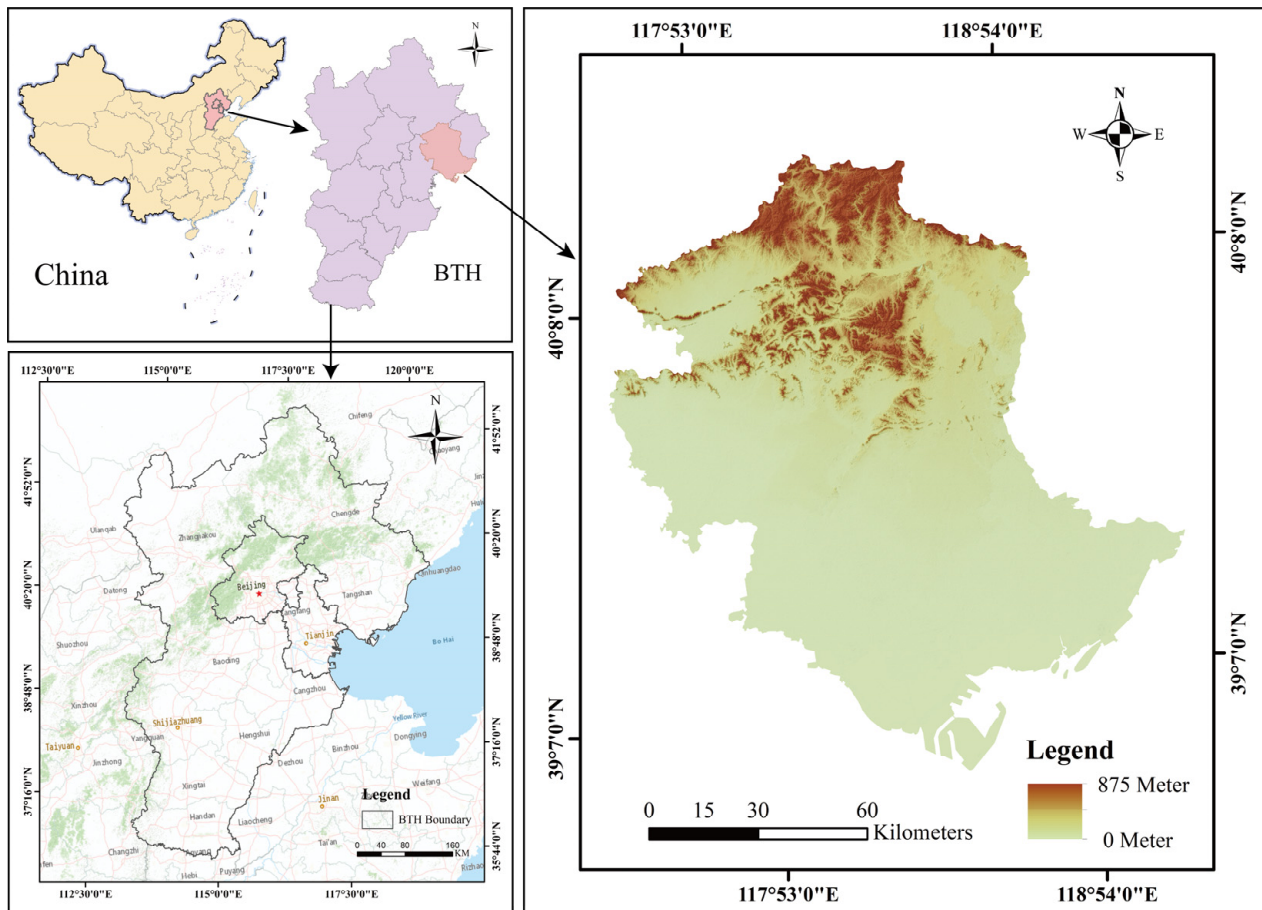


Figure 1. Location of BTH region.

In 2021, the total gross domestic product (GDP) of the BTH region reached approximately CNY 9.6 trillion, accounting for 8.43% of the national GDP [43]. The BTH region, as an essential base for China's manufacturing and modern industry, has attracted many energy-intensive and highly polluting industries. It is facing severe environmental pollution problems [44,45]. Between October and December 2020, the average fine particulate matter ($PM_{2.5}$) concentration in Beijing, Tianjin, Hebei, and adjacent regions was restricted to less than $63 \mu\text{g}/\text{m}^3$ [46]. The average number of days of high pollution in these cities was limited to five days a year, yet the region continues to experience pronounced haze pollution [46].

2.2. Data Sources

2.2.1. SDGSAT-1 TIS Product

The SDGSAT-1 satellite is the first global sustainable satellite dedicated to the United Nations' 2030 Agenda for Sustainable Development Goals (SDGs) developed by the Chinese Academy of Sciences [47]. It carries three payloads: a multispectral imager (MII), a TIS, and a glimmer imager (GIU) [48]. Its primary objective is to investigate the interrelationship between human activities and the natural environment. SDGSAT-1 operates in a sun-synchronous orbit at an altitude of 505 km and an inclination of 97.5° , with a local time of

9:30 AM for the descending node and a revisit cycle of 11 days. The primary technical and performance indices of the SDGSAT-1 satellite are provided in Table 1.

Table 1. Technical and performance indices of SDGSAT-1.

Sensor Type	Wavelength (μm)	Spatial Resolution (m)	Imaging Swath Width (km)	Designed Radiometric Accuracy
MII	B1: 0.38~0.42 B2: 0.42~0.46 B3: 0.46~0.52 B4: 0.52~0.60 B5: 0.63~0.69 B6: 0.765~0.805 B7: 0.805~0.90	10	300	Relative: 2% Absolute: 5%
TIS	B1: 8~10.5 B2: 10.3~11.3 B3: 11.5~12.5	30	300	Relative: 5% Absolute: 1 K@300 K
GIU	P: 0.45~0.90 B: 0.43~0.52 G: 0.52~0.615 R: 0.615~0.69	10 40	300	Relative: 2% Absolute: 5%

The TIS is currently China's highest-resolution civil on-orbit thermal infrared imager and it exhibits the world's highest swath-to-resolution ratio [49]. It provides three infrared bands, namely, B1 (8.0~10.5 μm), B2 (10.60~11.19 μm), and B3 (10.50~12.51 μm) [50], and can detect differences with an accuracy for the noise equivalent differential temperature (NEDT) of less than 0.041 K @ 300 K at a spatial resolution of 30 m. The TIS is more precise than the Landsat satellite, which provides an NEDT of 0.047 K @ 300 K, with a 100 m spatial resolution, and it outperforms the MODIS, which provides an NEDT of 0.05 K @ 300 K, with a 1000 m spatial resolution [51]. During the commissioning phase of the TIS, analysis revealed that the NEDT values for the B1, B2, and B3 bands were 0.034, 0.047, and 0.076 K, respectively [52]. Specifically, the B1 band exhibits fewer strip noise issues (i.e., signal fluctuations in sensor scans caused by detector noise) than the other two bands (B2 and B3) [53]. The B2 and B3 bands are commonly used for retrieving surface temperatures in two split-window channels. In contrast, the B1 band is not typically used in infrared observational missions. The B1 band, exhibiting a wavelength range of 8.0–10.5 μm , is often used in combination with the B2 and B3 bands to enhance the accuracy of the surface temperature estimation through the application of a three-channel, split-window algorithm [52]. Liu et al. showed that the three-band approach outperforms the two-band method, achieving a root-mean-square error of less than 1 K [54].

Considering that the integration of the above three bands enables more precise surface temperature inversion and environmental monitoring, all three bands of the SDGSAT-1 TIS were used in this study for industrial heat source detection. Nighttime data are more accurate for detecting heat sources than daytime data because of the relatively stable background conditions, and the influence of solar radiation on high-temperature objects is limited [38]. Therefore, SDGSAT TIS cloudless data were collected in the evening. Complete coverage of the BTH region by TIS data requires nine image scenes, and the corresponding information is provided in Table 2.

Table 2. Information on the satellite data and derived products used in this study.

SDGSAT-1 TIS		Landsat 8 OLI		Landsat 9 OLI		
Date and time (UTC)	3 January 2022	13:19:42	19 April 2022	02:53:12	28 March 2022	02:41:45
		13:19:13		02:53:36		02:41:22
		13:18:43	26 April 2022	02:59:44	2 April 2022	03:00:42
	20 February 2022	13:31:21		02:59:20	18 April 2022	02:59:22
		13:30:51	3 May 2022	03:05:57	22 May 2022	02:47:54
		13:30:21		03:05:33		02:47:30
		13:30:21	21 May 2022	02:54:31		02:47:06
	25 April 2023	13:18:19		02:54:07		02:46:43
		13:17:49	28 May 2022	03:00:17	27 May 2022	03:06:26
		30 May 2022	02:48:21			

2.2.2. Landsat 8/9 OLI Product

The Landsat 8 and 9 satellites were launched on 11 February 2013 and 27 September 2021, respectively [55,56]. Landsat 8 carries the OLI with a spatial resolution of 30 m and a TIS with a 100 m resolution, while Landsat 9 carries OLI-2 and TIRS-2. The Landsat 8/9 constellation operates in a sun-synchronous orbit at an altitude of 705 km and an inclination of 98.2°, with a revisit cycle of 16 days. The radiometric resolution of Landsat 8 is 12 bits, that of Landsat 9 is 14 bits, and the area covered by each Landsat 8/9 image scene is 185 × 185 km² [57]. Landsat 8/9 satellite information is listed in Table 3. Landsat 8/9 data can be applied in various scientific domains, such as environmental monitoring, agriculture, and urban planning, offering essential information for Earth observation.

Table 3. Information on the Landsat 8/9 satellite system.

Items		Parameters				
Landsat satellite		8			9	
Launch		11 February 2013			27 September 2021	
Sensors		OLI/TIRS			OLI-2/TIRS-2	
Revisit cycle		16 d			16 d	
Width		185 km			185 km	
Radiometric resolution (bits)		12			14	
Spectral (spatial) resolution	Pan	500~680 nm	15 m	Pan	500~680 nm	15 m
	Blue	433~453 nm	30 m	Blue	430~450 nm	30 m
		450~515 nm			450~510 nm	
	Green	525~600 nm		Green	530~590 nm	
	Red	630~680 nm		Red	640~670 nm	
	Near infrared (NIR)	845~885 nm		NIR	850~880 nm	
	Shortwave infrared (SWIR)	1560~1660 nm		SWIR	1570~1650 nm	
		1360~1390 nm			1360~1380 nm	
		2100~2300 nm			2110~2290 nm	
	TIRS	10,600~11,190 nm	100 m	TIRS	10,600~11,190 nm	100 m
		11,500~12,510 nm			11,500~12,510 nm	

In 2017, the U.S. Geological Survey (USGS) adopted Collection for data, software, and algorithm update management and reprocessed all the archived Landsat data, including Landsat-8 data, into the Collection-1 (C1) format. In December 2020, the USGS updated and reprocessed the entire Landsat archive to conform to the Collection-2 (C2) format. Landsat 8/9 C2 Level-2 products are created by applying extra corrections to Level-1 products to eliminate atmospheric effects that vary over time, space, and spectrum. Level-2 data can be directly adopted in quantitative research applications, while Level-1 data, which are subjected only to geometric rectification, necessitate radiometric calibration for use in scientific studies [58]. Landsat 8/9 OLI data are suitable for detecting industrial heat sources because they exhibit the same spatial resolution as SDGSAT-1 TIS data and a stable data quality. Therefore, we chose 19 image scenes from the Collection-2 Level-2 product that were temporally aligned with SDGSAT-1 TIS data and exhibited a cloud coverage lower than 10% to achieve comprehensive spatial coverage of the entire BTH region.

2.2.3. POI Data

Geospatial big data, represented by POIs, provide new concepts for studying the urban spatial distribution and structure [59]. Notably, points, lines, and area structures with categorical attributes are used to abstractly express geographical entities such as factories and supermarkets [60]. Currently, POI data can be obtained from various mapping services and social media platforms, such as Google Maps, AutoNavi, Baidu Maps, Yelp, and Foursquare [61]. These platforms provide a wealth of geographical information resources that are extensively used in various fields, ranging from business analytics to urban planning. In this paper, POI data obtained from the Amap database via an open application programming interface (API) (<https://lbs.amap.com/api/webservice/guide/api/search>, (accessed on 29 August 2023)) are used to classify industrial heat source objects. Amap is one of the largest web-mapping, navigation, and location-based service (LBS) platforms in China; it hosts a vast and detailed database that includes geographical information, road networks, POI information, and various traffic data. The Amap POI database provides comprehensive and categorized data for various POIs in China, such as dining services, shopping facilities, entertainment and leisure facilities, cultural and educational institutions, public facilities, financial and insurance facilities, real estate facilities, companies and enterprises, transportation facilities, and medical and healthcare service facilities. This study utilizes POI data specifically from the category of companies and enterprises.

2.2.4. Auxiliary Data

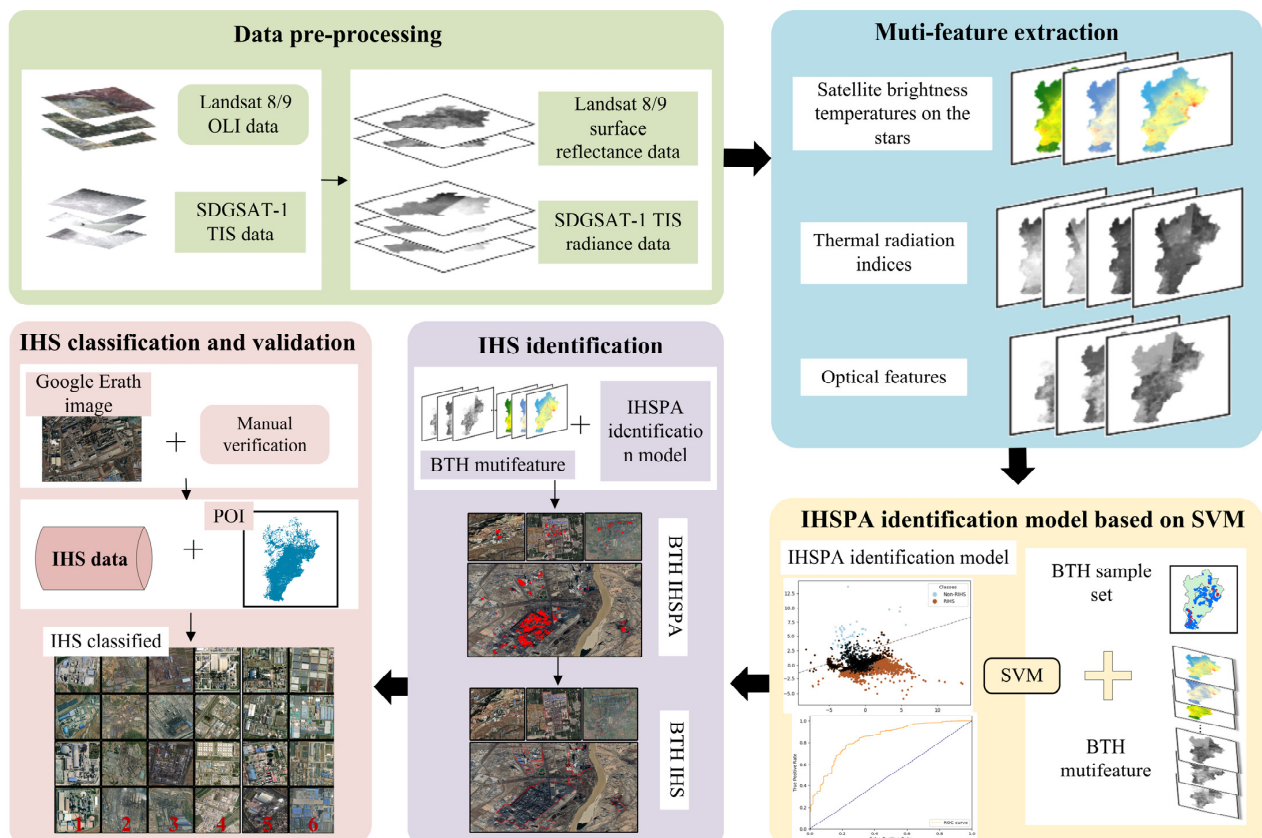
The coordinate system used for the spatial calculations and analyses was the standard Universal Transverse Mercator coordinate system of 50°N based on the WGS84 datum. High-resolution (0.5 m) optical images acquired from Google Earth were used to identify the main production areas and validate the reliability of the industrial heat source products. The NPP-VIIRS active-fire/hotspot (ACF) dataset was used for comparative data analysis and to determine the operational statuses of industrial heat sources. Two industrial heat source inventories from Ma [30] and Liu [29] were adopted for comparison with the detection results. The information for the datasets used in this paper is presented in Table 4.

2.3. Methods

The framework of the workflow in this paper is shown in Figure 2. The workflow includes five steps: data preprocessing, multifeature extraction, model construction for industrial heat source production area identification, industrial heat source and production area identification, and industrial heat source classification and validation.

Table 4. Information on the datasets used in this paper.

Dataset Name		Period	Resolution	Website
SDGSAT-1 TIS product		2022–2023	30 m	http://124.16.184.48:6008 (accessed on 2 July 2023)
Landsat 8/9 OLI product		2022	30 m	https://www.usgs.gov (accessed on 3 July 2023)
POI data		2023	Points	open API of Gaode Maps (https://lbs.amap.com/api/webservice/guide/api/search (accessed on 29 August 2023))
NPP-VIIRS active-fire/hotspot data (ACF)		2022	375 m	https://firms.modaps.eosdis.nasa.gov/ (accessed on 9 September 2023)
High-resolution optical images		/	0.5 m	Google Earth (https://www.google.cn (accessed on 8 July 2023))
Industrial heat source datasets	Liu’s datasets	2018	Polygon	https://doi.org/10.1016/j.rse.2017.10.019 (accessed on 9 October 2023)
	Ma’s datasets	2018	Polygon	https://doi.org/10.3390/su10124419 (accessed on 7 July 2023)
BTH administrative divisions		2020	Polygon	https://www.webmap.cn (accessed on 18 June 2023)

**Figure 2.** Framework of this study. IHS indicates an industrial heat source, and IHSPA indicates an industrial heat source production area.

2.3.1. Data Preprocessing

A reduced geometric positioning error contributes to enhancing the accuracy of image analysis and processing. The SDGSAT-1 TIS L4A/L4B products and Landsat 8/9 OLI C2 Level-2 science products (L2SP) used in this study have already been geometrically corrected [62]. Radiometric calibration, a basic processing step for remote sensing images, involves converting the digital numbers (DNs) captured by satellite sensors into metrics such as the radiance, reflectance, or brightness temperature at the sensor level [63].

In this study, radiometric calibration based on parameters sourced from the data file was employed to convert the SDGSAT-1 TIS data. The spectral radiance of the SDGSAT-1 TIS data was calculated using Equation (1):

$$L_{\lambda i} = ML_i * Qcal_i + AL_i, \quad (1)$$

where $L_{\lambda i}$ is the spectral radiance value of the i th band ($W/(m^2 \times sr \times \mu m)$); i denotes the band identification number of the SDGSAT-1 TIS; ML_i and AL_i are the gain and migration parameters, respectively, which can be obtained from the corresponding *.calib.xml file; and $Qcal_i$ is the DN value of the band.

To derive surface reflectance values from the Landsat 8/9 OLI C2 Level-2 data, the reflectance data should be multiplied by a scaling factor of 0.0000275 and then increased by a constant of -0.2 [64].

2.3.2. Multifeature Extraction

In this study, seven thermal features and three optical features were extracted to distinguish industrial heat source production areas and nonindustrial heat source production areas in the BTH region. Although thermal features are the most prominent characteristic of industrial heat source production areas, relying solely on these features is insufficient for distinguishing industrial heat source production areas from water bodies and roads. Research has indicated that optical features, based on the visible and near-infrared spectral range characteristics of an object or area, can support the effective differentiation of various land cover types [65]. Therefore, thermal and optical features were combined to identify industrial heat source production areas.

1. Thermal Features

The designed thermal features included the satellite brightness temperature and thermal radiation indices. The satellite brightness temperature comprises three parts: the atmospheric upward radiation brightness, the real radiation brightness of the ground after passing through the atmosphere to reach the satellite sensor, and the energy reflected by the downward atmospheric radiation that reaches the ground [66]. The satellite brightness temperatures of the thermal infrared bands within the atmospheric windows are similar to the actual surface temperatures [67]. The three bands of the SDGSAT-1 TIS are all located within the atmospheric windows. Therefore, the SDGSAT-1 TIS satellite brightness temperature can, to a certain extent, reflect the relative surface temperatures of different cover types on the Earth's surface. The satellite brightness temperature of each band of the SDGSAT-1 TIS can be calculated with Equation (2):

$$SBT_{Bi} = \frac{hc}{\lambda_i \times k \times \ln\left(1 + \frac{2hc^2}{L_{\lambda i} \times u^5}\right)}, \quad (2)$$

where SBT_{Bi} is the satellite brightness temperature of the i th band of the SDGSAT-1 TIS (K); h is the Planck's constant ($6.626 \times 10^{-34} J \cdot s$); and k is the Boltzmann's constant ($1.38 \times 10^{-23} J/S$). Moreover, c is the speed of light in a vacuum ($2.998 \times 10^8 m/s$), and λ_i is the central wavelength of the emitted radiation band (i) (μm).

Due to the temporal differences in the SDGSAT-1 TIS data used in this study and considering the spatial distribution characteristics of industrial heat source production areas, a normalization method was used to mitigate or eliminate the effects of varying times and seasons without changing the spatial distribution of the data [39]. This approach can accurately reflect the spatial distribution characteristics of industrial heat source production areas, as expressed in Equation (3):

$$SBT_{Br} = \frac{SBT_{Ba} - SBT_{Bmin}}{SBT_{Bmax} - SBT_{Bmin}}, \quad (3)$$

where SBT_{Br} is the relative SBT_B , SBT_{Ba} is the absolute SBT_B , and SBT_{Bmin} and SBT_{Bmax} are the minimum and maximum SBT_B values, respectively.

Four thermal radiation indices (RIs) were proposed using both the satellite brightness temperature and the near-infrared band of the Landsat 8/9 OLI to characterize the temperature difference between given industrial heat source production areas and the background. First, in industrial heat source production areas, the thermal radiation intensity in Band 2 was greater than that in Band 1, and the thermal radiation intensity in Band 1 was greater than that in Band 3. Then, RI_1 and RI_2 were constructed to highlight the differences among these three bands and balance the influence of the atmospheric conditions using normalized difference indices. The RI_1 and RI_2 formulas combine the use of SBT_{B1} , SBT_{B2} , and SBT_{B3} , which enhance the intensity of the thermal radiation from industrial heat sources in different wavelength bands and background regions. To enhance the differences in land cover types among these three bands and increase the sensitivity of the NIR band to changes in different feature characteristics, a reflectance value based on the NIR was introduced to construct RI_3 and RI_4 , which are similar to the thermal anomaly index (TAI) [68]. These indices can be calculated as follows:

$$RI_1 = \frac{SBT_{B2} - SBT_{B1}}{SBT_{B2} + SBT_{B1}}, \quad (4)$$

$$RI_2 = \frac{SBT_{B3} - SBT_{B1}}{SBT_{B3} + SBT_{B1}}, \quad (5)$$

$$RI_3 = \frac{SBT_{B2} - SBT_{B1}}{\rho_{nir}}, \quad (6)$$

$$RI_4 = \frac{SBT_{B3} - SBT_{B1}}{\rho_{nir}}, \quad (7)$$

where SBT_{B1} , SBT_{B2} , and SBT_{B3} are the satellite brightness temperatures of Bands 1, 2, and 3, respectively, of the SDGSAT-1 TIS, and ρ_{nir} is the reflectance value based on the NIR band of the Landsat 8/9 OLI data.

2. Optical Features

While thermal characteristics are the primary features of industrial heat sources, water bodies and certain land surfaces with high heat capacities also experience relatively high temperatures and thermal radiation at night [69]. Therefore, relying solely on thermal characteristics may not aid in effectively distinguishing between industrial and nonindustrial heat sources. Hence, additional features must be incorporated to enhance the differentiation between industrial heat sources and background areas. Optical features possess unique advantages in differentiating surface cover types. The integrated application of thermal and optical features can significantly enhance the identification and distinction capabilities of industrial heat sources and their background areas, thereby optimizing the accuracy of monitoring and analysis.

The optical features mainly include color, texture, shape, and spectral information [70]. These features are commonly used in fields such as image analysis and interpretation, object identification, and environmental monitoring [71,72]. The normalized difference vegetation index (NDVI), normalized difference built-up index (NDBI), and normalized difference water index (NDWI), which are derived from analyzing reflectance values at different wavelengths, are three important and widely applied optical feature indices used to analyze and monitor various aspects of the Earth's surface [73,74]. Therefore, these typical spectral information features (NDVI, NDBI, and NDWI) were used to distinguish industrial heat source production areas from other land cover types in this study, aiming to accurately identify industrial heat source production areas. Because the SDGSAT-1MII data do not provide the mid-infrared band information needed for calculating the NDBI, stable Landsat 8/9 OLI data with the same spatial resolution as that of the SDGSAT-1 TIS data

were chosen to extract the features of the NDVI, NDBI, and NDWI. These optical features can be calculated as follows:

$$\text{NDVI} = (\rho_{\text{nir}} - \rho_{\text{r}}) / (\rho_{\text{nir}} + \rho_{\text{r}}), \quad (8)$$

$$\text{NDBI} = (\rho_{\text{swir}} - \rho_{\text{nir}}) / (\rho_{\text{swir}} + \rho_{\text{nir}}), \quad (9)$$

$$\text{NDWI} = (\rho_{\text{g}} - \rho_{\text{nir}}) / (\rho_{\text{g}} + \rho_{\text{nir}}), \quad (10)$$

where ρ_{nir} , ρ_{r} , ρ_{swir} , and ρ_{g} are the reflectance values based on the near-infrared, red, mid-infrared, and green bands, respectively, of the Landsat 8/9 OLI data.

2.3.3. Industrial Heat Source Production Area Identification Model Based on SVM

An SVM is a powerful mathematical computational model used for classification tasks. As supervised learning models, SVMs (with a strong statistical foundation and high efficiency) have been used in both the regression and classification fields [75]. They can map the input sample space to a high-dimensional feature space using core mapping, which allows them to overcome traditional machine learning issues, such as dimensional disasters and overfitting problems [76]. Additionally, they provide significant benefits for resolving small-sample, nonlinear, and high-dimensional identification problems. Therefore, an SVM was used to construct an industrial heat source production area identification model. First, sample points from the BTH region, including industrial heat source production area (positive) and nonindustrial heat source production area (negative) samples, were established using SDGSAT-1 satellite brightness temperature and high-resolution images. Industrial heat source production area samples corresponded to anomaly points with high thermal radiation according to SDGSAT-1 satellite brightness temperature data in industrial areas. The nonindustrial heat source production area (negative) samples corresponded to background areas. Then, multiple features of the sample points, as outlined in Section 2.3.2, were extracted. Second, an industrial heat source production area identification model was developed based on an SVM using the sample set, with the training and test samples randomly distributed at an 8:2 ratio. The training samples were utilized for model construction, while the test samples were employed to evaluate the quality and reliability of the model. Finally, an industrial heat source production area identification model was constructed for BTH.

2.3.4. Industrial Heat Source and Production Area Identification

In the process of heat source and production area identification, there were two steps. First, industrial heat source production areas in the BTH region were identified using the industrial heat source production area identification model and multiple features of the BTH region. The identified industrial heat source production areas were production facilities or production areas at factories in operation. In addition, a single factory may comprise multiple industrial heat source production areas, and identifying industrial heat sources was necessary to obtain a comprehensive list of factories. Therefore, industrial heat source objects were generated based on topological correlation and the identification of industrial heat source production areas. Finally, the industrial heat source objects were obtained through manual screening and verification using Google Earth images.

2.3.5. Industrial Heat Source Classification and Validation

The identified industrial heat source objects were classified and validated by POI data and high-resolution image data. First, 310,879 valid POI data points were obtained and filtered based on the “company enterprise” category. Then, the place name attributes of the POIs were assigned to the industrial heat source objects based on the spatial relationship between the POI data and industrial heat source objects. Based on the keywords of the place names and widely used industrial classification standards in China, the industrial heat source objects were divided into six categories: cement plants, steel plants, coal chemical

plants, oil and gas development plants, thermal power plants, and other plants. The keywords used are listed in Table 5.

Table 5. Keywords used for industrial heat source categorization.

Category	Keywords				
Cement plants	Cement				
Steel plants	Steel	Foundry	Smelting	Casting	Metal products
Coal chemical plants	Coal chemical	Coking	Coke making	Coal	Coal gas
Oil and gas development plants	Petroleum	Natural gas	Energy	Petrochemical	Chemical industry
Thermal power plants	Thermal power				
Other plants	New energy	Building materials	Lime	Concrete	...

Finally, the identification and classification results for the industrial heat source objects were manually verified based on Google Earth and historical images. The remote sensing image characteristics of the different categories of industrial heat source objects are as follows, and examples of the objects of each type are shown in Figure 3: (1) Cement plants: Cement plants are often located in mountainous areas where stone mining can easily be performed. Generally, the production facilities of cement plants include raw material storage yards, crushing workshops, raw material silos, clinker silos, calcining facilities (shafts and rotary kilns), cement silos, etc. (2) Steel plants: the production facilities of steel plants generally include sintering facilities, ironmaking facilities, steel-rolling areas, storage areas, gas storage tanks, and others. (3) Coal chemical plants: Coal chemical plants are typically located in areas rich in coal and have convenient transportation infrastructure and an abundant energy supply. The operational areas at coal chemical plants generally include coal preparation areas, coking zones, purification zones, and dry-quenching areas. (4) Oil and gas development plants: Oil and gas development plants are generally located away from residential areas. The production areas of these plants primarily include coking areas, crude-oil tank areas, boiler sections, catalytic cracking zones, hydrogenation processing areas, etc. (5) Thermal power plants: Thermal power plants usually operate near cities or industrial zones to facilitate energy transmission and minimize energy loss. The production facilities mostly include combustion chambers, boilers, steam turbines and generators, cooling towers, and electrical and thermal transmission facilities. (6) Other plants: Other plants encompass all industrial heat sources that do not fall within the previously mentioned five categories; these plants cover a wide range of production activities across various industries, such as new energy plants and building material factories. Moreover, this category includes factories for which the heat source category cannot be determined due to the absence of POI data or the insufficient resolution of remote sensing images.

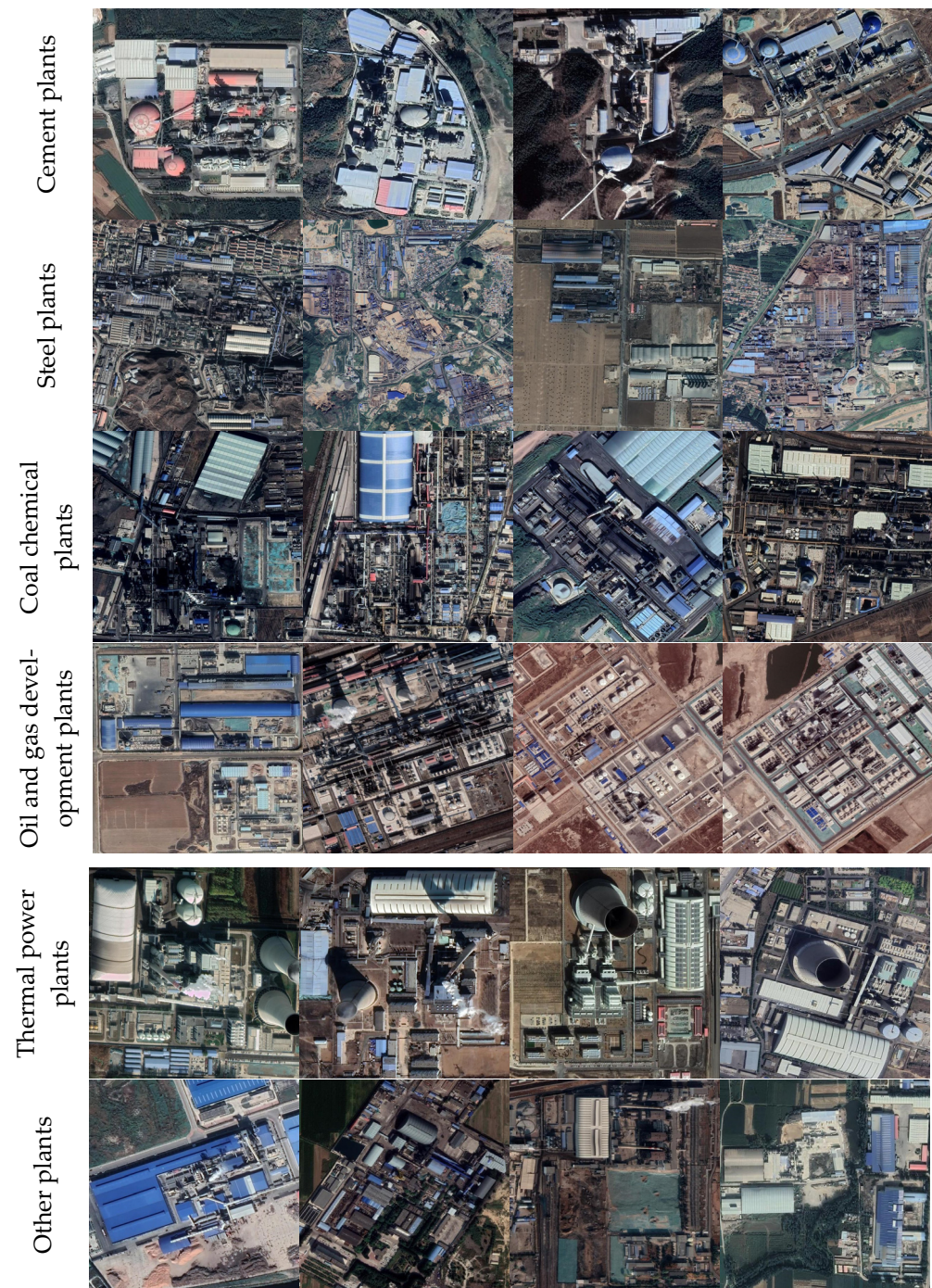


Figure 3. Remote sensing images of different types of industrial heat sources.

3. Results

3.1. Validation of Industrial Heat Source Production Areas Identified Using Multiple Features and SVM

To validate the effectiveness of identifying industrial heat source production areas using multiple features and an SVM, we conducted experiments with five different sets of feature combinations, as detailed in Table 6. The Landsat 8/9 optical features (L8/9 OFs) were only from Landsat 8/9 OLI data; the Landsat 8/9 temperature features (L8/9 TFs) were only from Landsat 8/9 TIRS data; the SDGSAT-1 thermal features (SDG TFs) were only from SDGSAT-1 TIS data; the Landsat 8/9 optical and temperature features (L8/9 OFs and TFs) were both from Landsat 8/9 OLI and TIRS data; and the Landsat 8/9 optical features and SDGSAT-1 thermal features (L8/9 OFs and SDG TFs) were from Landsat 8/9

OLI data and SDGSAT-1 TIS data. The L8/9 TF was the surface temperature derived from Landsat 8/9 Band 10.

Table 6. Information for different combinations of features.

Feature Combination	Abbreviation	Features
Landsat 8/9 optical features	L8/9 OFs	NDVI, NDBI, NDWI
Landsat 8/9 temperature features	L8/9 TFs	$T_{L8/9}$
SDGSAT-1 thermal features	SDG TFs	SBT_{Br1} , SBT_{Br2} , SBT_{Br3} , RI_1 , RI_2 , RI_3 , RI_4
Landsat 8/9 optical and temperature features	L8/9 OFs and TFs	NDVI, NDBI, NDWI, $T_{L8/9}$
Landsat 8/9 optical features and SDGSAT-1 thermal features	L8/9 OFs and SDG TFs	NDVI, NDBI, NDWI, SBT_{Br1} , SBT_{Br2} , SBT_{Br3} , RI_1 , RI_2 , RI_3 , RI_4

In this paper, 3443 sample points were produced, with 1131 sample points from nonindustrial heat source production areas. The 3443 sample points were divided into test and training samples, of which approximately 688 sample points were included in the test sample set. For each classification experiment, the accuracy of the trained model was assessed based on four metrics: the producer's accuracy (PA), user's accuracy (UA), overall accuracy (OA), and kappa coefficient (K). The OA is frequently employed to quantify the proportion of correctly classified pixels, offering a direct measure of the model precision, whereas the K provides an essential statistical evaluation of the classification performance beyond chance levels [77].

Table 7 and Figure 4 show the accuracy and visual results obtained in different feature combination experiments. Table 7 shows that the L8/9 OF and SDG TF combinations had the highest OA (90.96%) and K (0.79) compared to the other feature combinations. Additionally, these combinations exhibited a high PA, enabling the effective and accurate detection of industrial heat sources in production areas. As illustrated in Figure 4, the L8/9 OF and SDG TF combinations were more effective at distinguishing industrial heat source production areas from background areas than the other feature combinations were. Although some building surfaces associated with industrial heat sources can be identified solely from Landsat optical features, this approach fails to pinpoint the actual production area locations of factories, leading to missed factories with heat emissions. Furthermore, the SDG TF misidentifies high-temperature water as an industrial heat source. In summary, combining thermal features from the SDGSAT-1 TIS with optical features from Landsat 8/9 OLI data enables the effective and accurate identification of production area locations and industrial heat sources (as mentioned in Section 2.3.2).

Table 7. The producer's accuracy (PA), user's accuracy (UA), overall accuracy (OA), and kappa coefficient (K) values for different feature combination experiments.

Feature Combination	PA	UA	OA	K
L8/9 OFs	80.00	3.77	69.97	0.05
L8/9 TFs	72.81	72.81	81.92	0.59
SDG TFs	95.51	64.89	85.42	0.67
L8/9 OFs and TFs	77.39	79.46	85.71	0.72
L8/9 OFs and SDG TFs	98.86	74.36	90.96	0.79

3.2. Analysis of Industrial Heat Source Detection and Identification Results for BTH

A total of 793 industrial heat source objects (shown in Figure 5) were identified in this study. A total of 748 objects were manually confirmed as real industrial heat source objects based on Google Earth images, reflecting an identification accuracy of 94.33%. Most of the nonindustrial heat source objects are located in Hebei Province, accounting for 91.11% of the total number of nonindustrial heat sources (41). These data included buildings and abandoned sites with thermal anomalies. In addition, the industrial heat source objects are

mainly concentrated in the eastern part of Hebei, especially in the Tangshan area and in the southeastern parts of Beijing and Tianjin.

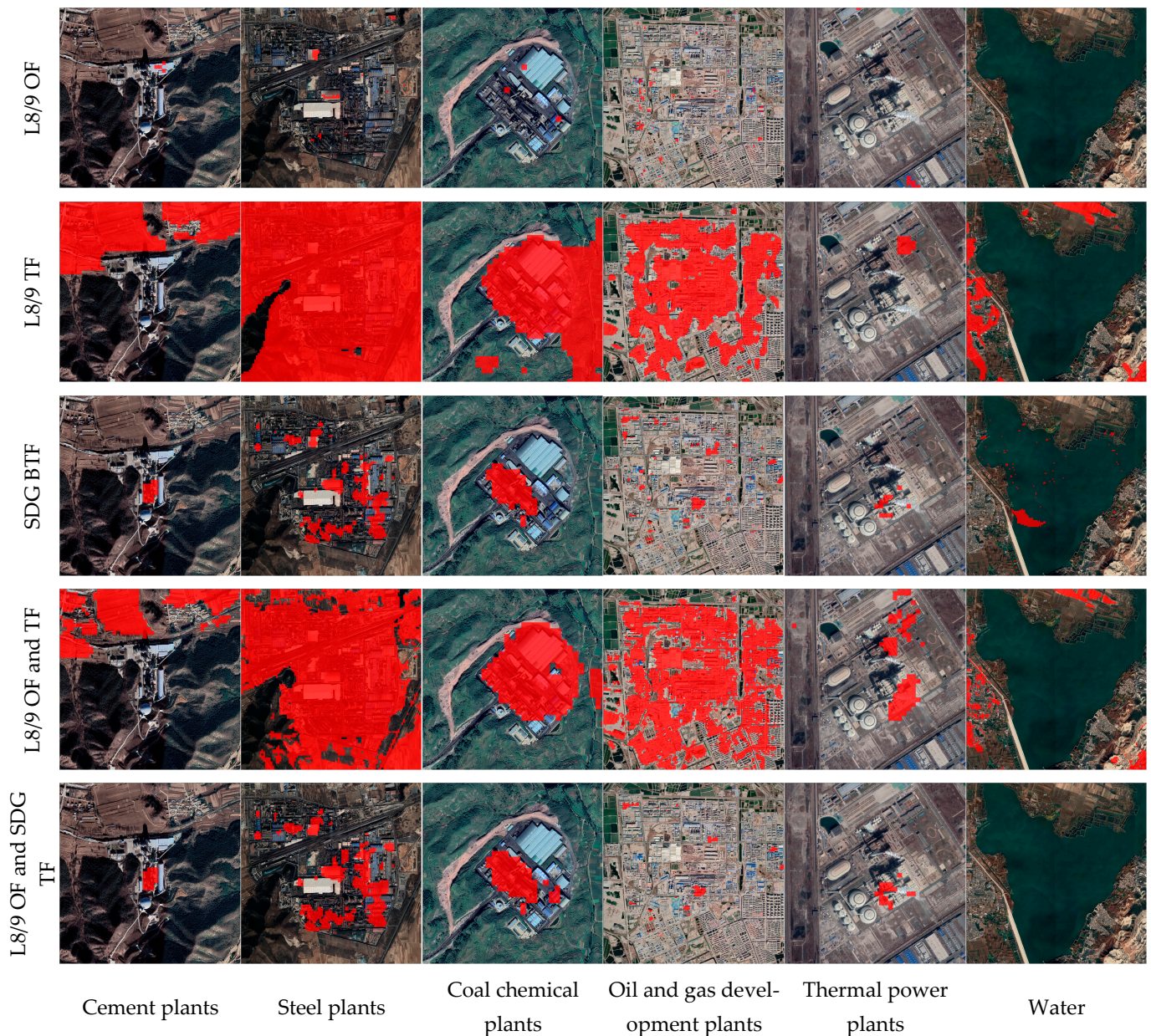


Figure 4. Visualization of the identification of five typical industrial heat source production areas and a typical water body (marked red mask) using different combinations of features.

3.3. Analysis of Industrial Heat Source Classification and Identification Results for BTH

Through the methods described in Section 2.3.4 and remote sensing image characteristic classification for the industrial heat sources, a total of 748 real industrial heat sources were categorized into six types. The spatial distribution and a statistical analysis of the classification results are shown in Figures 6 and 7, respectively. In the BTH region, 354 plants fall in the “other plants” category, accounting for 47.33% of the total number of plants. In addition, there are 130 steel plants (17.38%), 121 oil gas development plants (16.18%), 60 cement plants (8.02%), 53 thermal power plants (7.09%), and 30 coal chemical plants (4.01%) in the BTH region. Excluding the “other plants” category, steel plants are the most common, accounting for 32.99% of these five types of factories, followed by oil and gas development plants, with a proportion of 30.71%.

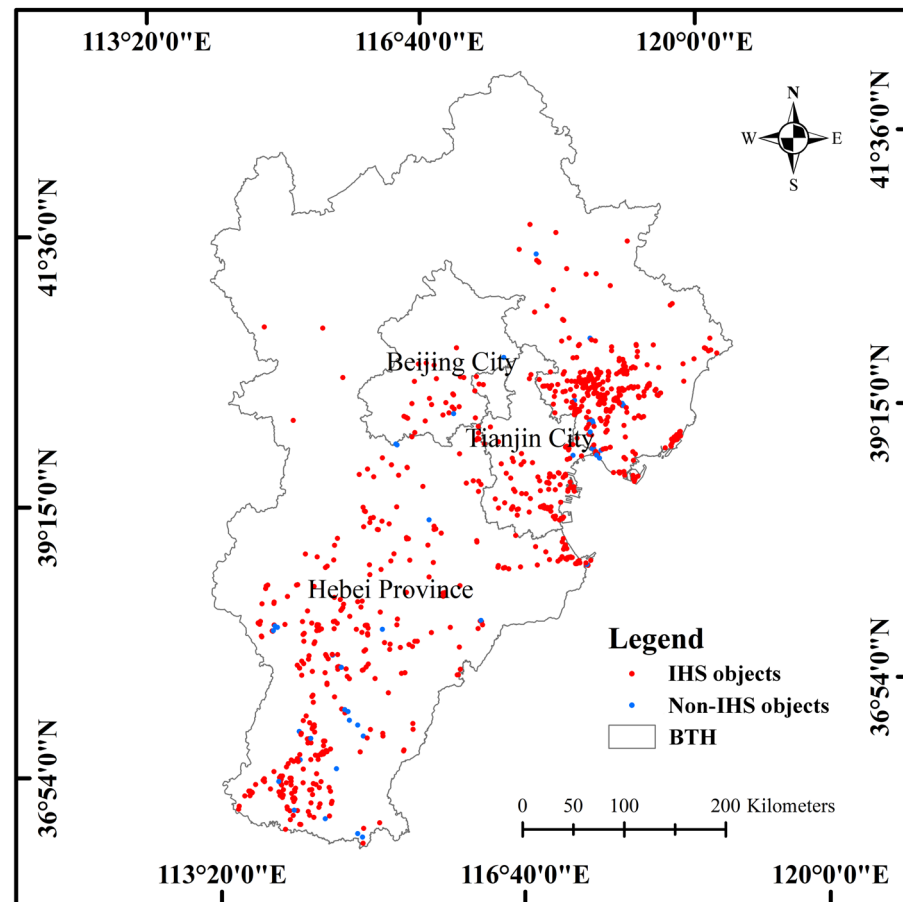


Figure 5. Spatial distributions of industrial heat sources and nonindustrial heat sources in BTH region.

3.4. Spatial Distribution Characteristics of Industrial Heat Source Identification Results in BTH Region

3.4.1. Spatial Distribution Characteristics of Industrial Heat Sources at Provincial Scale

The spatial distribution of the industrial heat source identification results at the provincial scale is shown in Figure 8a. In the BTH region, the real industrial heat source objects are predominantly located in Hebei Province, totaling 640, accounting for 85.56% of all identified objects. All of the identified coal chemical plants are located in Hebei Province. Cement plants account for as much as 95% of the total number of factories in this category, while steel factories account for 89.23%. Tianjin ranks second, with 83 real industrial heat source objects (10.59%). Among them, oil and gas development factories account for the highest percentage of the total number of factories in this category, at 22.31%. However, in Beijing, there are 25 real industrial heat source objects, accounting for 3.34% of the total number of industrial heat sources. Among them, other plants account for the highest percentage of the total number of factories in this category in Beijing, at 4.52%. Hebei Province is rich in coal, oil, and iron and has a relatively high number of steel factories. Tianjin's mineral resources largely include coal and oil. The primary mineral resources in Beijing are anthracite and iron.

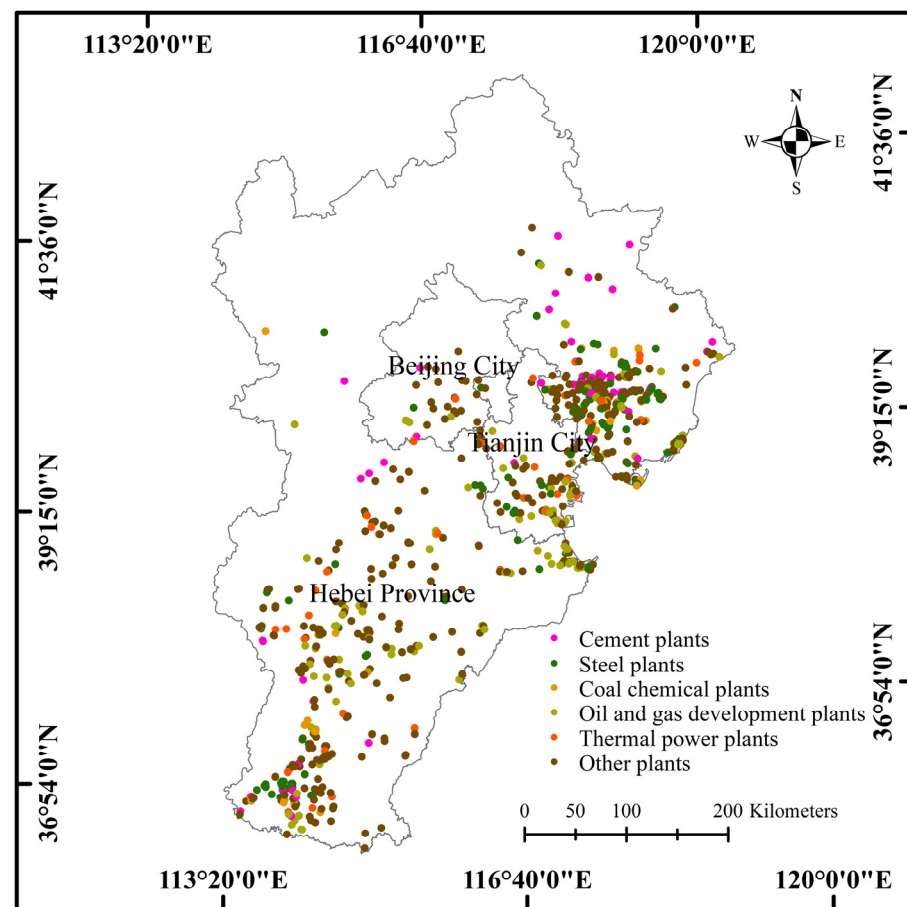


Figure 6. Spatial distribution of cement plants, steel plants, coal chemical plants, oil and gas development plants, thermal power plants, and other plants.

3.4.2. Spatial Distribution Characteristics of Industrial Heat Sources at Municipal Scale

The spatial characteristics of the municipal-scale industrial heat source objects in the study area are shown in Figure 8b, and the specific quantities for each city category are shown in Table 8. Based on the concentration of the industrial heat sources, the cities can be categorized into five levels: low (the number of industrial heat sources is in the range of 0~4), relatively low (5~28), medium (29~58), medium-high (59~84), and high (85~261) concentrations. (1) In the BTH region, the industrial heat sources are mainly concentrated in the Tangshan–Tianjin and Shijiazhuang–Xingtai–Handan regions, revealing a spatial distribution pattern of high values in the southeast and low values in the northwest. (2) The total number of industrial heat source objects in the cities at the medium-high concentration level is the largest, accounting for 40.61% of the total number of heat source objects identified in this paper, and the numbers in Tianjin and Handan (84) are the largest among the studied cities. (3) With 261 industrial heat sources, Tangshan has significantly more heat objects than other cities (the only city at the high-concentration level), as it is an important industrial base in China. Zhangjiakou, Chengde, Xingtai, and Handan are mature resource-based cities, while Tangshan is a regenerative resource-based city. These cities possess relatively mature and stable industrial and resource support systems, serving as crucial bases for ensuring China's energy resource security at present. However, industry advancement unavoidably leads to atmospheric pollution. This significantly contributes to PM_{2.5} transport from heavily industrialized cities, such as Tangshan, Shijiazhuang, and from Handan to Beijing.

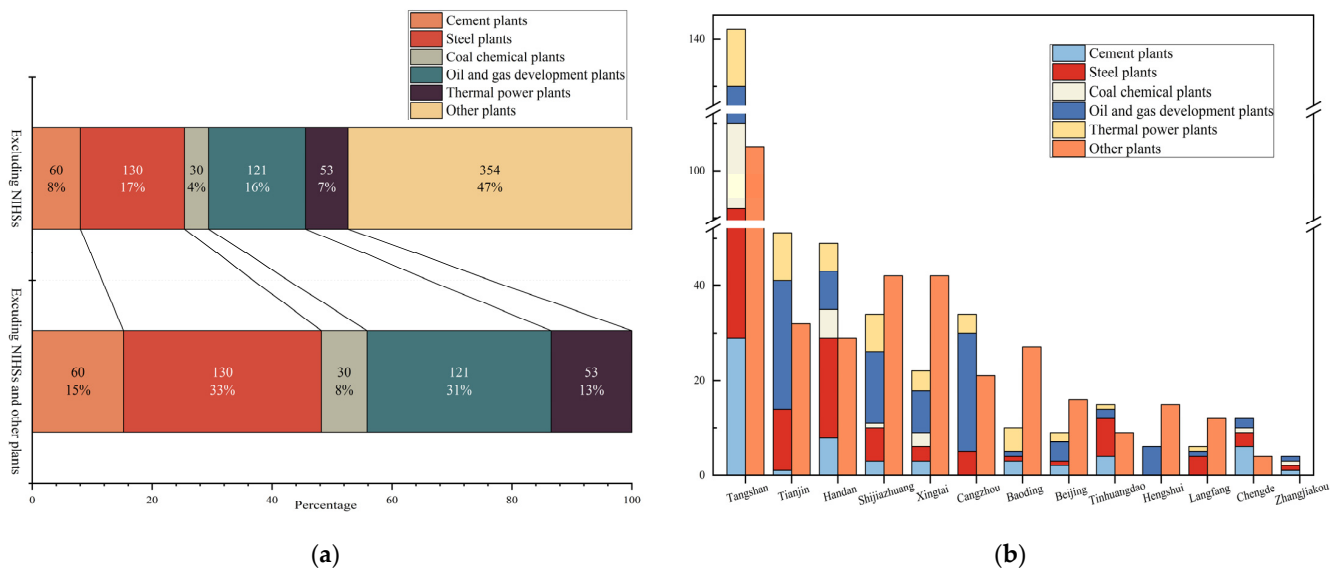


Figure 7. Industrial heat source classification results: (a) percentage of classification results excluding (1) nonindustrial heat sources (NIHSs) and (2) nonindustrial heat sources (NIHSs) and other plants; (b) distribution of six categories in each municipality of BTH region.

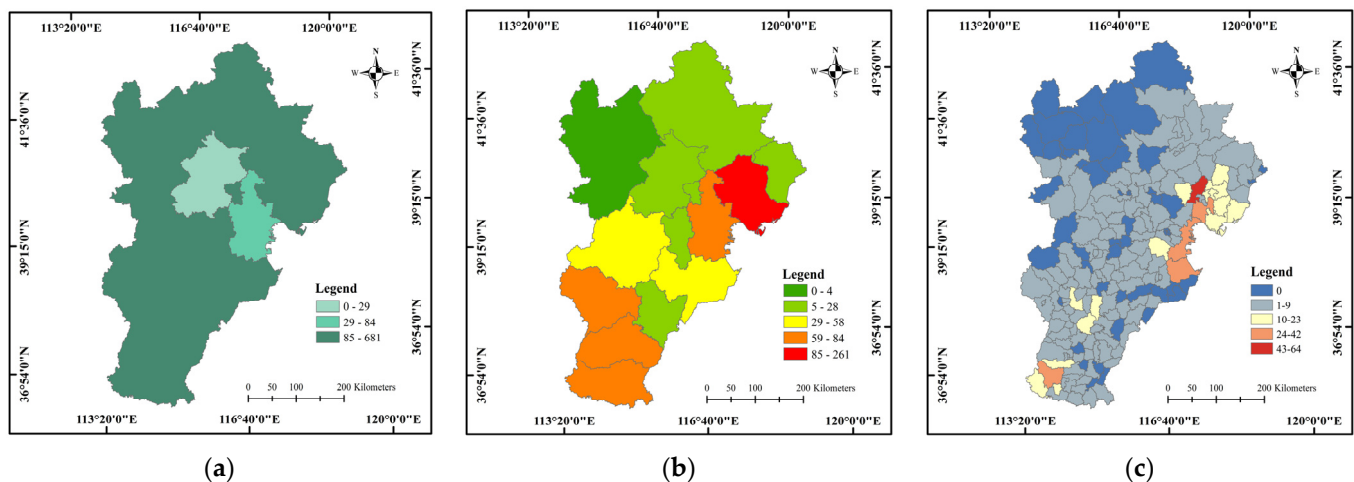


Figure 8. Spatial distribution of industrial heat source objects at various scales: (a) provincial scale; (b) municipal scale; (c) county scale.

Most of the cement plants are concentrated in Tangshan and Handan. The majority of the steel plants are located in Tangshan, Handan, and Tianjin. The coal chemical plants are primarily found in Tangshan and Handan, with very few or no coal chemical plants found in the other cities. The oil and gas development plants are mainly distributed across Tianjin, Cangzhou, Tangshan, and Shijiazhuang. The thermal power plants are mainly located in Tangshan, Tianjin, and Shijiazhuang. Most of the other plants are located in Tangshan, totaling 105, accounting for 14.04% of the total number of plants. In Zhangjiakou, there are no other plants. Tangshan is a well-known steel base, and, excluding other plants, steel plants account for 44.37% of the total number of factories in Tangshan, followed by cement plants at 20.42%. In 2021, the total steel production in Tangshan city reached 131 million tons, ranking first in China.

Table 8. Specific number of factories in each category in each city.

	Cement Plants	Steel Plants	Coal Chemical Plants	Oil and Gas Development Plants	Thermal Power Plants	Other Plants	Sum
Tangshan	29	63	18	20	12	105	247
Tianjin	1	13	0	27	10	32	83
Handan	8	21	6	8	6	29	78
Shijiazhuang	3	7	1	15	8	42	76
Xingtai	3	3	3	9	4	42	64
Cangzhou	0	5	0	25	4	21	55
Baoding	3	1	0	1	5	27	37
Beijing	2	1	0	4	2	16	25
Qinhuangdao	4	8	0	2	1	9	24
Hengshui	0	0	0	6	0	15	21
Langfang	0	4	0	1	1	12	18
Chengde	6	3	1	2	0	4	16
Zhangjiakou	1	1	1	1	0	0	4
Sum	60	130	30	121	53	354	748

3.4.3. Spatial Distribution Characteristics of Industrial Heat Sources at County Scale

The county-scale industrial heat source identification results are shown in Figure 8c. According to these results, the industrial heat sources in the BTH region exhibit a locally clustered pattern, with a high density in several counties along the coast and a few counties in the southern region. Based on the distribution of the number of industrial heat sources, the 200 counties in the BTH region can be divided into five levels: none (the number of industrial heat sources is 0) and low (1~9), medium (10~23), medium–high (24~42), and high (43~64) concentrations. The 54 counties without industrial heat sources are located primarily in the northwestern regions of Zhangjiakou–Chengde–Baoding and the southeastern region of Cangzhou. This may be due to resource scarcity, policy constraints, or geographic limitations that limit industrial development. The 126 counties at the low-concentration level are distributed across the central and southern parts of the BTH region, encompassing 361 industrial heat sources, which account for 45.52% of the total number of pollutants. The 15 counties at the medium-concentration level largely occur in the southeastern part of Tangshan, the eastern part of Shijiazhuang, and the western part of Handan. The four counties at the medium–high-concentration level include Wuan (28) in Handan, Huanghua (33) in Cangzhou, Fengnan District (36) in Tangshan, and the Binhai New Area (42) in Tianjin. Fengrun District in Tangshan city is classified at the high-concentration level, with 64 industrial heat sources, accounting for 8.07% of the total number of heat sources in the study region. Notably, there are many industrial heat sources scattered around Tangshan, revealing a spatial pattern of central clustering–external enclosure.

In Tangshan’s Fengrun District, the number of other plants is the largest, with 22 industrial heat source objects. There are no coal chemical factories in Fengrun District. There are 22 fewer industrial heat source objects in Tianjin’s Binhai New Area than in Fengrun District. According to the identification results, there are no cement, steel, or coal chemical plants in the Binhai New Area, with oil and gas development plants being the most common, accounting for 17.36% of the total number of plants in this category.

4. Discussion

4.1. Effectiveness of Industrial Heat Source Production Area Detection Based on Nighttime SDGSAT-1 TIS Data Compared to Other TIS Data

To analyze the effectiveness of the industrial heat source production area detection based on nighttime TIS data, low-resolution (ACF data, 375 m), medium-resolution (Landsat 8/9 TIRS data, 100 m), and high-resolution (SDGSAT-1 TIS data, 30 m) daily data were compared. Then, the thermal radiation characteristics of the obtained industrial heat source production areas (as shown in Figure 9) were analyzed for the Donghua Steel Plant using

four datasets. Figure 9a shows a hotspot density map constructed from the ACF data between 1 January and 31 December 2022. Notably, although there is a clear thermal radiation phenomenon at the Donghua Steel Factory, production areas cannot be distinguished from the background. Figure 9c was constructed based on the temperature data from Band 10 of the Landsat 8 TIRS product on 1 May 2023. In this case, there is a pronounced increase in thermal radiation at the Donghua Steel Factory. However, the areas with concentrated thermal radiation predominantly exhibit smooth surface covers. Additionally, Figure 9d,e show the day- and nighttime satellite brightness temperature distributions based on the SDGSAT-1TIS data. During the daytime, the Donghua Steel Factory exhibits a distinct aggregation of thermal radiation, as shown in Figure 9d, which indicates that these data can capture the thermal radiation surface boundaries of buildings more precisely than Landsat 8 data can. However, the high-temperature areas mostly exhibit smooth surface covers, resulting in considerable fluctuations in the brightness temperature. In contrast, the nighttime data in Figure 9e clearly indicate that the thermal radiation at the Donghua Steel Factory is concentrated in the major production areas, such as the sintering, iron, and steel zones. Moreover, areas such as storage sections, gas storage tanks, and residential areas do not exhibit prominent thermal radiation aggregation. In summary, high-spatial-resolution TIS data can accurately reflect changes in thermal radiation for different land cover types. The nighttime SDGSAT-1 TIS data more accurately reflect the operational statuses of industrial heat sources. Therefore, these data constitute the best choice for effectively detecting industrial heat source production areas.

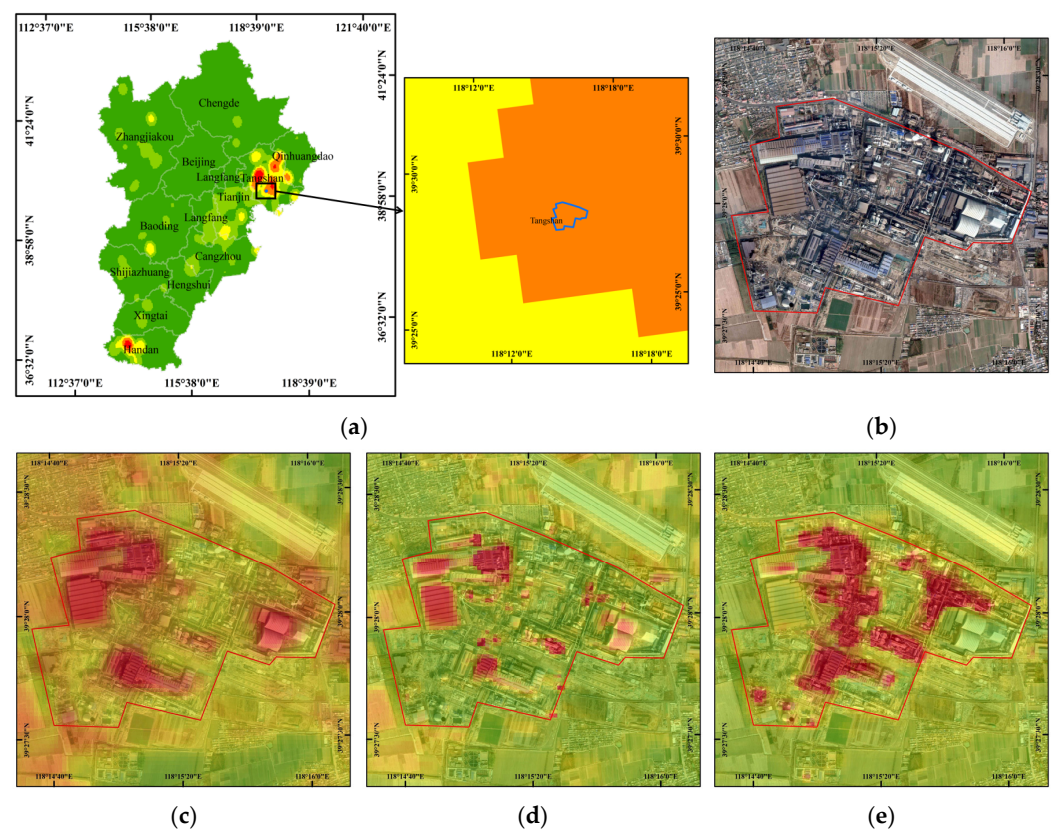


Figure 9. (a) Distribution of ACF kernel densities around Donghua Steel Plant in 2022. (b) Image of Donghua Steel Plant from Google Earth on 8 November 2022. (c) Landsat 8 TIRS Band 10 temperature distribution for 1 May 2023, at Donghua Steel Plant. (d) Distribution of satellite brightness temperature based on SDGSAT-1 TIS Band 1 during daytime on 30 March 2023. (e) Distribution of satellite brightness temperature based on SDGSAT-1 TIS Band 1 during nighttime on 25 April 2023. Note: in the figures, the colors range from green to red, with redder colors indicating higher thermal radiation.

4.2. Analysis of Spatial Distribution of Brightness Temperature Using Nighttime SDGSAT-1 TIS Data for Different Categories of Industrial Heat Sources

To reveal the spatial distributions of the brightness temperatures of the different categories of industrial heat sources, the plant areas were divided into production and nonproduction areas based on high-resolution Google Earth images and the brightness temperatures determined from nighttime SDGSAT-1 TIS data (Figure 10). Most heat is generated in production areas during production-related processes. Nonproduction areas include material storage areas and residential and administrative areas, among others, which do not generate a significant amount of heat in the factory production process. Additionally, buildings, vegetation, cultivated land, grasslands, and bare land near the obtained plants were extracted to serve as background areas. Table 9 indicates the following results: (1) The production areas of cement plants exhibit the highest brightness temperatures, reaching 301.78 K; these areas are primarily distributed in calcination zones (vertical/rotary kilns). The maximum brightness temperature in the production areas of cement plants is approximately 35.70 K greater than that in the background areas (buildings). (2) The production areas of thermal power plants exhibit the lowest brightness temperatures, averaging 277.31 K; these areas are predominantly associated with combustion chambers, cooling towers, boilers, electrical sections, and heat transfer equipment. The maximum brightness temperature in the production areas of thermal power plants is 2.30 K greater than that in the nonproduction areas and 2.96 K greater than that in the background areas (buildings). (3) The maximum brightness temperature in the production areas of steel plants is 292.31 K, a value mainly observed in the sintering, iron, and steel areas. The maximum brightness temperature in the entire production area of steel plants is approximately 9.49 K lower than that in the corresponding area of cement plants, while the minimum brightness temperatures are roughly similar. (4) The mean brightness temperature in the production area of coal chemical plants is 280.84 K, a value mainly observed in coking areas. The overall brightness temperature in the production area of coal chemical factories is slightly greater (by 2.68 K) than that in the corresponding area of steel factories. (5) The production areas of oil and gas development plants are mainly the coking and blast furnace areas. The maximum brightness temperature in the production areas of oil and gas development plants is 283.81 K, which is 7.20 K greater than that in the nonproduction areas and 7.26 K greater than that in the background areas (building area). The maximum, minimum, and average brightness temperatures in the nonproduction areas of oil and gas development plants are the highest overall.

4.3. Comparison with Existing Industrial Heat Source Data

To validate the accuracy and precision of our generated dataset, our results were compared with the industrial heat source datasets created by Ma [16] using ACF data (updated to 2021) and Liu [29,78] using the VIIRS VNF product (updated to 2017). In addition, 493 and 242 industrial heat source objects were obtained in the BTH region. Then, 469 (95.13%, 493/469) and 229 (94.62%, 229/242) RIGHS objects were manually verified using high-resolution Google Earth images and POI data. Considering the relevant policies involving structural adjustment and production capacity reduction proposed in 2015 and the air pollution control policy introduced in 2013 [79], some factories were converted into other uses or shut down in the BTH region. Notably, only 214 and 108 industrial heat sources were still in operation in 2022 according to the ACF point data between January 1 and 31 December 2022. More comparison details are shown in Figure 11 and Table 10. The comparison results indicate that our dataset provides significant improvements in the number, scale, and spatial overlap of identified objects (Figure 10b). (1) Our method yields many more actual industrial heat source objects (748) and operational industrial heat sources—nearly 3.50 times more—than that (214) reported by Ma, and 6.93 times more than that reported by Liu (108). (2) The total area of industrial heat sources identified with our method was 552.01 km², which was 8.9% larger than the area identified by Ma (506.76 km²) and 27.45% smaller than the area identified by Liu (703.52 km²). Additionally, the average

identification area based on our results was 0.7 km², while those of Ma and Liu were 1.03 and 2.91 km², respectively. This suggests that the industrial heat sources detected by our method are more precise, with a smaller number and smaller total area. (3) The spatial overlap of our results was greater than those for the other two datasets. Our results exhibit an overlap of 82.24% (176/214) with Ma's data, which have 57.57% greater coverage than our data (185/750). In addition, a 67.86% increment in overlap was obtained when comparing our results with Liu's data.



Figure 10. Google Earth images and satellite brightness temperatures based on SDGSAT-1 TIS Band 1 for different categories of industrial heat sources: (a) Jinyu Jidong Cement Pingquan Company

(Chengde, China); (b) Tangshan Jidong Cement Plant (Tangshan, China); (c) Anfeng Steel Company (Qinhuangdao, China); (d) Ruifeng Steel Group (Tangshan, China); (e) Tangshan Baoliyuan Coking Co., Ltd. (Tangshan, China); (f) Tangshan Dafeng Coking Co., Ltd. (Tangshan, China); (g) Tianjin Weierke Petrochemical Company (Tianjin, China); (h) China Petroleum Dagang Petrochemical Company (Tianjin, China); (i) Hebei Datang International Fengrun Thermal Power Co., Ltd. (Tangshan, China); and (j) Hebei JianTou Zunhua Thermal Power Co., Ltd. (Tangshan, China).

Table 9. Different categories of industrial heat source brightness temperature information.

Category	Maximum Brightness Temperature (K)			Minimum Brightness Temperature (K)			Mean Brightness Temperature (K)		
	PA	N-PA	PA-NPA	PA	N-PA	PA-NPA	PA	N-PA	PA-NPA
Cement plants	301.78	275.32	26.46	274.76	264.32	10.44	282.47	271.25	11.22
Steel plants	292.31	276.12	16.19	274.10	269.51	4.59	278.16	272.77	5.38
Coal chemical plants	294.82	275.78	19.03	275.23	270.38	4.85	280.84	273.90	6.94
Oil and gas development plants	283.81	276.61	7.20	275.38	270.94	4.44	277.61	275.12	2.49
Thermal power plants	277.31	275.01	2.30	273.88	270.08	3.80	275.70	273.00	2.70

Notably, 563 industrial heat source objects identified in this paper were not recognized by Ma, and 625 such objects were not identified by Liu. In particular, 53 thermal power plants detected by our method were not identified by Liu. The only thermal power plant identified by Ma was erroneously classified as a steel industrial heat source object. This difference might be due to the lower heat emissions in the production areas of thermal power plants, which typically have brightness temperatures less than approximately 278 K, relative to those of other types of industrial heat sources. Consequently, the production areas of thermal power plants cannot be detected based on ACF and VNF data. Although our method yielded a larger number of industrial heat source objects, some plants were correctly identified by Ma and Liu but were missed by our approach. The primary reason for these missed detections was that the SDGSAT-1 TIS product associates comparatively lower temperatures with these objects, differing from the temperatures of high-heat emissions from industrial heat sources, making these sources difficult to identify with our model.

4.4. Study Significance and Uncertainties

Our method integrates SDGSAT-1 TIS data and Landsat 8/9 OLI data, enhancing the precision and granularity of the identification of industrial heat sources. Compared to traditional methods based on thermal anomaly data, our method employs SDGSAT-1 TIS data with a higher spatial resolution and temperature sensitivity, allowing for the identification of more low-temperature emissions and small-scale industrial heat sources. Additionally, this approach enables the precise detection of the production areas in factories. This study is the first to introduce SDGSAT-1 TIS data into industrial heat source monitoring, demonstrating its potential application value in environmental monitoring and industrial emission analysis.

This research has several limitations. First, due to the lack of inversion parameters for retrieving land surface temperatures (LSTs) from SDGSAT-1 thermal infrared data, this study could not utilize LSTs, which accurately reflect the thermal characteristics of industrial heat sources. Second, the classification accuracy of industrial heat source data is affected by the absence or inaccuracy of the POI data, as source classification is based on POI data. Future research could focus on inverting more accurate surface temperatures to improve the identification accuracy. Additionally, the combination of other land features or data for classifying industrial heat sources, rather than relying solely on POI and high-resolution data, could be explored.

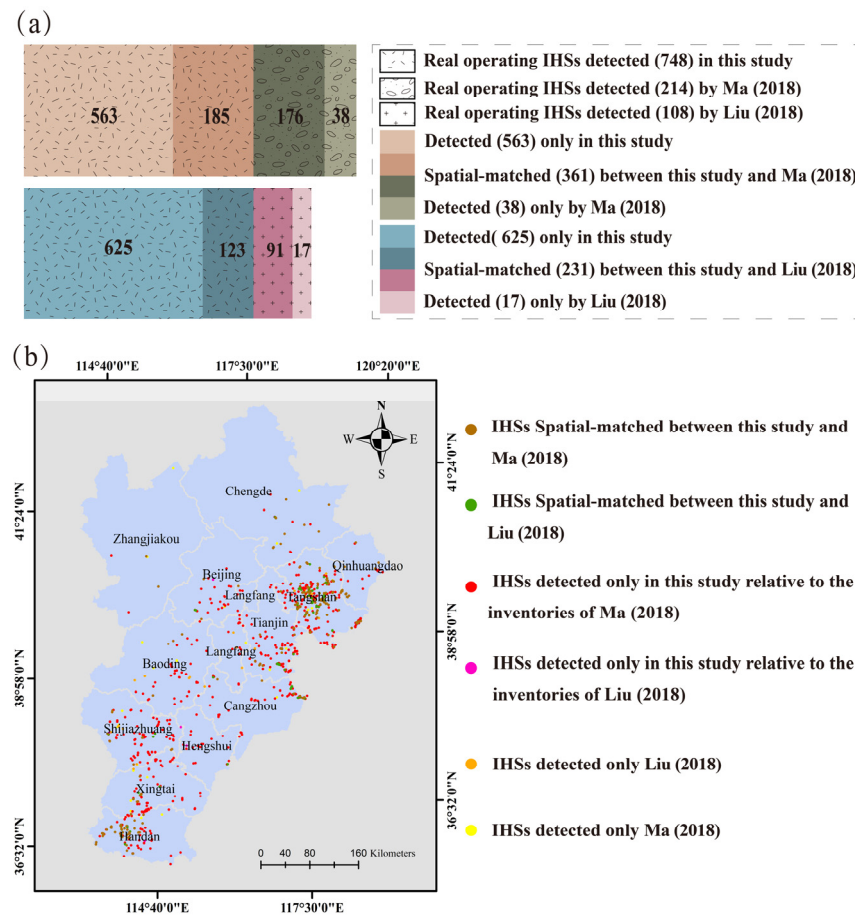


Figure 11. Comparison of our results with the real and operating IHSs (industrial heat sources) detected by Ma et al. [30] and Liu et al. [29]. (a) Statistical comparison of the three datasets. (b) Comparison of the spatial distributions of the matches and mismatches among the three datasets.

Table 10. A comparison of the industrial heat sources identified using the method described in this study with Ma's inventory based on active-fire-point data [30] and Liu's inventory based on night-fire data [29]. For comparison, Ma's and Liu's datasets were synchronized to 2022.

	Updated Year	Industrial Heat Sources Detected	Real Industrial Heat Sources	Accuracy	Closed	Real and Operating Industrial Heat Sources	Total Area (km ²)	Average Area (km ²)
Our results	2022	793	748	94.33%	/	748	552.01	0.7
Ma's inventory	2021	493	469	95.13%	255	214	506.76	1.03
Liu's inventory	2017	242	229	94.62%	121	108	703.53	2.91

5. Conclusions

The accurate identification and categorization of industrial heat sources and production areas are crucial for effective energy management, heat emission and environmental pollution monitoring, and global climate change mitigation. However, existing methods cannot be used to accurately identify industrial heat source production areas, and they fail to recognize industrial heat sources with low-heat emissions and small areas. In this study, a new industrial heat source production area identification and industrial heat source classification model using SDGSAT-1 TIS and Landsat 8/9 OLI data was proposed to improve the accuracy and granularity of industrial heat source recognition. Then, industrial heat sources and production areas in the BTH region were accurately identified and classified. The following conclusions are drawn from this study:

1. The use of SDGSAT-1 TIS thermal features combined with Landsat 8/9 OLI optical features for identifying industrial heat sources significantly enhances the distinction between production and background areas while also providing high accuracy and visual quality;
2. Compared to the ACF data (375 m) and Landsat 8/9 TIRS data (100 m), the nighttime SDGSAT-1 TIS data (30 m) can be used to more accurately detect industrial heat source production areas;
3. More than 2~6 times more industrial heat sources were detected in the BTH region using our model than were reported by Ma and Liu. Some industrial heat sources with low-heat emissions and small areas, such as 53 thermal power plants, were detected using TIS data but were not in the other cases;
4. The industrial heat source objects were mainly concentrated in the Tangshan–Tianjin and Shijiazhuang–Xingtai–Handan regions, revealing a spatial distribution pattern of high values in the southeast and low values in the northwest;
5. The spatial distributions and statistical characteristics of the brightness temperature differed for the different categories of industrial heat sources. The production areas of the cement plants exhibited the highest brightness temperatures, reaching 301.78 K, while the thermal power plants exhibited the lowest brightness temperatures, averaging 277.31 K.

The research findings indicate that the identification method proposed in this paper can be used to precisely detect the production areas of plants and effectively identify industrial heat sources with low-heat emissions, resolving the issue of low granularity in the identification process. The results provide accurate information regarding production areas and regional positions, providing valuable data for industrial layout planning in the BTH region. Future work could focus on the more accurate classification of industrial heat source objects and the use of more accurate surface temperature data to identify industrial heat source production areas in much larger regions.

Author Contributions: Conceptualization, Y.X., C.M., Y.Z. and D.Y.; methodology, Y.X., C.M., Y.Z. and D.Y.; software, Y.X. and C.M.; validation, Y.X.; formal analysis, Y.X. and C.M.; investigation, Y.X., C.M., Y.Z., D.Y., B.C., X.H., H.C., B.F. and G.W.; resources, C.M.; data curation, Y.X., C.M., Y.Z., D.Y., B.C., X.H., H.C., B.F. and G.W.; writing—original draft preparation, Y.X., C.M. and Y.Z.; writing—review and editing, Y.X., C.M. and Y.Z.; visualization, Y.X. and C.M.; supervision, C.M., Y.Z. and D.Y.; project administration, C.M., Y.Z. and D.Y.; funding acquisition, C.M. and B.C. All authors have read and agreed to the published version of the manuscript.

Funding: This work was supported by the National Natural Science Foundation of China (No. 72073125), the China-Pakistan Joint Research Center of Earth Sciences, CAS-HEC, Islamabad 45320, Pakistan, and the Youth Innovation Promotion Association of the Chinese Academy of Science under Grant 2021126.

Data Availability Statement: The authors acknowledge the free use of Landsat 8/9 OLI products (<https://earthexplorer.usgs.gov/>, accessed on 3 July 2023). The SDGSAT-1 TIS data were kindly provided by the International Research Center of Big Data for Sustainable Development Goals (CBAS). SDGSAT-1 data developed and processed by the CBAS can be obtained free of charge following the approval of a CBAS proposal, with data provided through the SDGSAT-1 Open Science Program (<https://www.sdgsat.ac.cn/sciencePlan/aboutPro>, accessed on 27 June 2023).

Acknowledgments: The authors would like to thank the SDG BIGDATA Center and National Space Science Center for providing us with the data. The authors thank the editors and the three anonymous reviewers for their valuable comments, which helped improve the manuscript.

Conflicts of Interest: The authors declare no conflicts of interest.

References

1. Inayat, A. Current Progress of Process Integration for Waste Heat Recovery in Steel and Iron Industries. *Fuel* **2023**, *338*, 127237. [\[CrossRef\]](#)
2. Abdelkareem, M.A.; Maghrabie, H.M.; Sayed, E.T.; Kais, E.-C.A.; Abo-Khalil, A.G.; Radi, M.A.; Baroutaji, A.; Olabi, A.G. Heat Pipe-Based Waste Heat Recovery Systems: Background and Applications. *Therm. Sci. Eng. Prog.* **2022**, *29*, 101221. [\[CrossRef\]](#)
3. Bataille, C.G.F. Physical and Policy Pathways to Net-Zero Emissions Industry. *WIREs Clim. Chang.* **2020**, *11*, e633. [\[CrossRef\]](#)
4. Hao, Y.; Guo, Y.; Li, S.; Luo, S.; Jiang, X.; Shen, Z.; Wu, H. Towards Achieving the Sustainable Development Goal of Industry: How Does Industrial Agglomeration Affect Air Pollution? *Innov. Green Dev.* **2022**, *1*, 100003. [\[CrossRef\]](#)
5. Adebisi, F.M. Air Quality and Management in Petroleum Refining Industry: A Review. *Environ. Chem. Ecotoxicol.* **2022**, *4*, 89–96. [\[CrossRef\]](#)
6. Conejo, A.N.; Birat, J.-P.; Dutta, A. A Review of the Current Environmental Challenges of the Steel Industry and Its Value Chain. *J. Environ. Manag.* **2020**, *259*, 109782. [\[CrossRef\]](#) [\[PubMed\]](#)
7. Andrew, R.M. Global CO₂ Emissions from Cement Production. *Earth Syst. Sci. Data* **2018**, *10*, 195–217. [\[CrossRef\]](#)
8. Friedlingstein, P.; O'Sullivan, M.; Jones, M.W.; Andrew, R.M.; Gregor, L.; Hauck, J.; Le Quéré, C.; Luijkx, I.T.; Olsen, A.; Peters, G.P.; et al. Global Carbon Budget 2022. *Earth Syst. Sci. Data* **2022**, *14*, 4811–4900. [\[CrossRef\]](#)
9. Chatkin, J.; Correa, L.; Santos, U. External Environmental Pollution as a Risk Factor for Asthma. *Clin. Rev. Allerg. Immunol.* **2022**, *62*, 72–89. [\[CrossRef\]](#)
10. Xue, Y.; Wang, L.; Zhang, Y.; Zhao, Y.; Liu, Y. Air Pollution: A Culprit of Lung Cancer. *J. Hazard. Mater.* **2022**, *434*, 128937. [\[CrossRef\]](#)
11. Gourgiotis, A.; Kyvelou, S.S.; Lainas, I. Industrial Location in Greece: Fostering Green Transition and Synergies between Industrial and Spatial Planning Policies. *Land* **2021**, *10*, 271. [\[CrossRef\]](#)
12. Li, R.; Tao, M.; Zhang, M.; Chen, L.; Wang, L.; Wang, Y.; He, X.; Wei, L.; Mei, X.; Wang, J. Application Potential of Satellite Thermal Anomaly Products in Updating Industrial Emission Inventory of China. *Geophys. Res. Lett.* **2021**, *48*, e2021GL092997. [\[CrossRef\]](#)
13. Sarkar, A.; Chouhan, P. Modeling Spatial Determinants of Urban Expansion of Siliguri a Metropolitan City of India Using Logistic Regression. *Model. Earth Syst. Environ.* **2020**, *6*, 2317–2331. [\[CrossRef\]](#)
14. Morand, S.; Lajaunie, C. Outbreaks of Vector-Borne and Zoonotic Diseases Are Associated With Changes in Forest Cover and Oil Palm Expansion at Global Scale. *Front. Vet. Sci.* **2021**, *8*, 661063. [\[CrossRef\]](#) [\[PubMed\]](#)
15. Cheon, S.; Kim, J.-A. Quantifying the Influence of Urban Sources on Night Light Emissions. *Landsc. Urban Plan.* **2020**, *204*, 103936. [\[CrossRef\]](#)
16. Zhang, P.; Yuan, C.; Sun, Q.; Liu, A.; You, S.; Li, X.; Zhang, Y.; Jiao, X.; Sun, D.; Sun, M.; et al. Satellite-Based Detection and Characterization of Industrial Heat Sources in China. *Environ. Sci. Technol.* **2019**, *53*, 11031–11042. [\[CrossRef\]](#) [\[PubMed\]](#)
17. Elvidge, C.D.; Zhizhin, M.; Sparks, T.; Ghosh, T.; Pon, S.; Bazilian, M.; Sutton, P.C.; Miller, S.D. Global Satellite Monitoring of Exothermic Industrial Activity via Infrared Emissions. *Remote Sens.* **2023**, *15*, 4760. [\[CrossRef\]](#)
18. Taranik, J.V.; Coolbaugh, M.F.; Vaughan, R.G. An Overview of Thermal Infrared Remote Sensing with Applications to Geothermal and Mineral Exploration in the Great Basin, Western United States. In *Remote Sensing and Spectral Geology*; Bedell, R., Crósta, A.P., Grunsky, E., Eds.; Society of Economic Geologists: Littleton, CO, USA, 2009; Volume 16, ISBN 978-1-934969-13-7.
19. Junaidi, S.N.; Khalid, N.; Othman, A.N.; Hamid, J.R.A.; Saad, N.M. Analysis of the Relationship between Forest Fire and Land Surface Temperature Using Landsat 8 OLI/TIRS Imagery. *IOP Conf. Ser. Earth Environ. Sci.* **2021**, *767*, 012005. [\[CrossRef\]](#)
20. Coskuner, K.A. Assessing the Performance of MODIS and VIIRS Active Fire Products in the Monitoring of Wildfires: A Case Study in Turkey. *Iforest-Biogeosciences For.* **2022**, *15*, 85. [\[CrossRef\]](#)
21. McClain, E.P.; Pichel, W.G.; Walton, C.C. Comparative Performance of AVHRR-Based Multichannel Sea Surface Temperatures. *J. Geophys. Res. Ocean.* **1985**, *90*, 11587–11601. [\[CrossRef\]](#)
22. Xu, W.; Wooster, M.J.; He, J.; Zhang, T. First Study of Sentinel-3 SLSTR Active Fire Detection and FRP Retrieval: Night-Time Algorithm Enhancements and Global Intercomparison to MODIS and VIIRS AF Products. *Remote Sens. Environ.* **2020**, *248*, 111947. [\[CrossRef\]](#)
23. Flasse, S.P.; Ceccato, P. A Contextual Algorithm for AVHRR Fire Detection. *Int. J. Remote Sens.* **1996**, *17*, 419–424. [\[CrossRef\]](#)
24. Shi, K.; Touge, Y. Characterization of Global Wildfire Burned Area Spatiotemporal Patterns and Underlying Climatic Causes. *Sci. Rep.* **2022**, *12*, 644. [\[CrossRef\]](#)
25. Sathishkumar, V.E.; Cho, J.; Subramanian, M.; Naren, O.S. Forest Fire and Smoke Detection Using Deep Learning-Based Learning without Forgetting. *Fire Ecol.* **2023**, *19*, 9. [\[CrossRef\]](#)
26. Jethva, H. Assessing Predictability of Post-Monsoon Crop Residue Fires in Northwestern India. *Front. Earth Sci.* **2022**, *10*, 2473. [\[CrossRef\]](#)
27. Guo, Y.; Xiao, H.; Zhang, S.; Hao, D. Application of GIS Technology in Environmental Impact Assessment—Taking a Steel Plant as an Example. *Sci. Consult. (Decis. Manag.)* **2009**, 76–77. (In Chinese)
28. Chen, P.; Lu, L.; Zhu, H.; Zhu, Y.; Wang, Y. Research on the Suitability of Image at Different Resolutions for the Identification of Steel Enterprise Using Remote Sensing. *J. Geo-Inf. Sci.* **2015**, *17*, 1119–1127.
29. Liu, Y.; Hu, C.; Zhan, W.; Sun, C.; Murch, B.; Ma, L. Identifying Industrial Heat Sources Using Time-Series of the VIIRS Nightfire Product with an Object-Oriented Approach. *Remote Sens. Environ.* **2018**, *204*, 347–365. [\[CrossRef\]](#)

30. Ma, C.; Yang, J.; Chen, F.; Ma, Y.; Liu, J.; Li, X.; Duan, J.; Guo, R. Assessing Heavy Industrial Heat Source Distribution in China Using Real-Time VIIRS Active Fire/Hotspot Data. *Sustainability* **2018**, *10*, 4419. [\[CrossRef\]](#)
31. Lai, J.; Zhu, J.; Chai, J.; Xu, B. Spatial-Temporal Analysis of Industrial Heat and Productivity in China. *Appl. Geogr.* **2022**, *138*, 102618. [\[CrossRef\]](#)
32. Gemitzi, A.; Dalampakis, P.; Falalakis, G. Detecting Geothermal Anomalies Using Landsat 8 Thermal Infrared Remotely Sensed Data. *Int. J. Appl. Earth Obs. Geoinf.* **2021**, *96*, 102283. [\[CrossRef\]](#)
33. Ichi, E.; Dorafshan, S. Effectiveness of Infrared Thermography for Delamination Detection in Reinforced Concrete Bridge Decks. *Autom. Constr.* **2022**, *142*, 104523. [\[CrossRef\]](#)
34. Han, F.; Zhao, F.; Li, F.; Shi, X.; Wei, Q.; Li, W.; Wang, W. Improvement of Monitoring Production Status of Iron and Steel Factories Based on Thermal Infrared Remote Sensing. *Sustainability* **2023**, *15*, 8575. [\[CrossRef\]](#)
35. Baugh, K. Characterization of Gas Flaring in North Dakota Using the Satellite Data Product, VIIRS Nightfire. *AGU Fall Meet. Abstr.* **2015**, *2015*, A23N-05.
36. Elvidge, C.D.; Zhizhin, M.; Baugh, K.; Hsu, F.-C.; Ghosh, T. Methods for Global Survey of Natural Gas Flaring from Visible Infrared Imaging Radiometer Suite Data. *Energies* **2016**, *9*, 14. [\[CrossRef\]](#)
37. Tkachenko, N.; Tang, K.; McCarten, M.; Reece, S.; Kampmann, D.; Hickey, C.; Bayarara, M.; Foster, P.; Layman, C.; Rossi, C.; et al. Global Database of Cement Production Assets and Upstream Suppliers. *Sci. Data* **2023**, *10*, 696. [\[CrossRef\]](#)
38. Schroeder, W.; Oliva, P.; Giglio, L.; Csiszar, I.A. The New VIIRS 375m Active Fire Detection Data Product: Algorithm Description and Initial Assessment. *Remote Sens. Environ.* **2014**, *143*, 85–96. [\[CrossRef\]](#)
39. Zhou, Y.; Zhao, F.; Wang, S.; Liu, W.; Wang, L. A Method for Monitoring Iron and Steel Factory Economic Activity Based on Satellites. *Sustainability* **2018**, *10*, 1935. [\[CrossRef\]](#)
40. Huang, W.; Jiao, J.; Zhao, L.; Hu, Z.; Peng, X.; Yang, L.; Li, X.; Chen, F. Thermal Discharge Temperature Retrieval and Monitoring of NPPs Based on SDGSAT-1 Images. *Remote Sens.* **2023**, *15*, 2298. [\[CrossRef\]](#)
41. Li, L.; Zhou, X.; Hu, Z.; Gao, L.; Li, X.; Ni, X.; Chen, F. On-Orbit Monitoring Flying Aircraft Day and Night Based on SDGSAT-1 Thermal Infrared Dataset. *Remote Sens. Environ.* **2023**, *298*, 113840. [\[CrossRef\]](#)
42. Wang, Q.; Hu, Z.; Zou, L.; Chen, F. Lunar Surface Temperature and Emissivity Retrieval From SDGSAT-1 Thermal Imager Spectrometer. *IEEE Geosci. Remote Sens. Lett.* **2023**, *20*, 7000805. [\[CrossRef\]](#)
43. National Bureau of Statistics China Statistical Yearbook. 2022. Available online: <http://www.stats.gov.cn/sj/ndsj/2022/indexeh.htm> (accessed on 1 November 2023).
44. Shen, L.; Yang, Z.; Du, X.; Wei, X.; Chen, X. A Health Risk-Based Threshold Method to Evaluate Urban Atmospheric Environment Carrying Capacity in Beijing-Tianjin-Hebei (BTH) Region. *Environ. Impact Assess. Rev.* **2022**, *92*, 106692. [\[CrossRef\]](#)
45. Zhang, Z.; Zhao, X.; Mao, R.; Xu, J.; Kim, S.-J. Predictability of the Winter Haze Pollution in Beijing-Tianjin-Hebei Region in the Context of Stringent Emission Control. *Atmos. Pollut. Res.* **2022**, *13*, 101392. [\[CrossRef\]](#)
46. Zhou, J.; Yin, T.; Tian, J. Research on the Impact of Beijing-Tianjin-Hebei Electric Power and Thermal Power Industry on Haze Pollution. *Energy Rep.* **2022**, *8*, 1698–1710. [\[CrossRef\]](#)
47. Yu, B.; Chen, F.; Ye, C.; Li, Z.; Dong, Y.; Wang, N.; Wang, L. Temporal Expansion of the Nighttime Light Images of SDGSAT-1 Satellite in Illuminating Ground Object Extraction by Joint Observation of NPP-VIIRS and Sentinel-2A Images. *Remote Sens. Environ.* **2023**, *295*, 113691. [\[CrossRef\]](#)
48. Qi, L.; Li, L.; Ni, X.; Zhou, X.; Chen, F. On-Orbit Spatial Quality Evaluation of SDGSAT-1 Thermal Infrared Spectrometer. *IEEE Geosci. Remote Sens. Lett.* **2022**, *19*, 7507505. [\[CrossRef\]](#)
49. Li, X.; Li, L.; Zhao, L.; Jiao, J.; Jiang, L.; Yang, L.; Chen, F.; Sun, S. In-Orbit Geometric Calibration for Long-Linear-Array and Wide-Swath Whisk-Broom TIS of SDGSAT-1. *IEEE Trans. Geosci. Remote Sens.* **2023**, *61*, 1000214. [\[CrossRef\]](#)
50. Hu, Y.; Li, X.-M.; Dou, C.; Jia, G.; Hu, Z.; Xu, A.; Ren, Y.; Yan, L.; Wang, N.; Cui, Z.; et al. Absolute Radiometric Calibration Evaluation of the Thermal Infrared Spectrometer Onboard SDGSAT-1. *Int. J. Digit. Earth* **2023**, *16*, 4492–4511. [\[CrossRef\]](#)
51. Guo, H.; Dou, C.; Chen, H.; Liu, J.; Fu, B.; Li, X.; Zou, Z.; Liang, D. SDGSAT-1: The World's First Scientific Satellite for Sustainable Development Goals. *Sci. Bull.* **2023**, *68*, 34–38. [\[CrossRef\]](#) [\[PubMed\]](#)
52. Hu, Z.; Zhu, M.; Wang, Q.; Su, X.; Chen, F. SDGSAT-1 TIS Prelaunch Radiometric Calibration and Performance. *Remote Sens.* **2022**, *14*, 4543. [\[CrossRef\]](#)
53. Qiu, Y.; Li, X.-M.; Guo, H. Spaceborne Thermal Infrared Observations of Arctic Sea Ice Leads at 30m Resolution. *EGU sphere* **2023**, *17*, 2829–2849. [\[CrossRef\]](#)
54. Liu, W.; Li, J.; Zhang, Y.; Zhao, L.; Cheng, Q. Preflight Radiometric Calibration of TIS Sensor Onboard SDG-1 Satellite and Estimation of Its LST Retrieval Ability. *Remote Sens.* **2021**, *13*, 3242. [\[CrossRef\]](#)
55. Ye, X.; Ren, H.; Zhu, J.; Fan, W.; Qin, Q. Split-Window Algorithm for Land Surface Temperature Retrieval From Landsat-9 Remote Sensing Images. *IEEE Geosci. Remote Sens. Lett.* **2022**, *19*, 7507205. [\[CrossRef\]](#)
56. Adiri, Z.; Lhissou, R.; El Harti, A.; Jellouli, A.; Chakouri, M. Recent Advances in the Use of Public Domain Satellite Imagery for Mineral Exploration: A Review of Landsat-8 and Sentinel-2 Applications. *Ore Geol. Rev.* **2020**, *117*, 103332. [\[CrossRef\]](#)
57. Wulder, M.A.; Roy, D.P.; Radeloff, V.C.; Loveland, T.R.; Anderson, M.C.; Johnson, D.M.; Healey, S.; Zhu, Z.; Scambos, T.A.; Pahlevan, N.; et al. Fifty Years of Landsat Science and Impacts. *Remote Sens. Environ.* **2022**, *280*, 113195. [\[CrossRef\]](#)

58. Herrick, C.; Steele, B.G.; Brentrup, J.A.; Cottingham, K.L.; Ducey, M.J.; Lutz, D.A.; Palace, M.W.; Thompson, M.C.; Trout-Haney, J.V.; Weathers, K.C. lakeCoSTR: A Tool to Facilitate Use of Landsat Collection 2 to Estimate Lake Surface Water Temperatures. *Ecosphere* **2023**, *14*, e4357. [\[CrossRef\]](#)
59. Xue, B.; Xiao, X.; Li, J.; Xie, X. Analysis of Spatial Economic Structure of Northeast China Cities Based on Points of Interest Big Data. *Sci. Geogr. Sin.* **2020**, *40*, 691–700.
60. Yu, C.; Ren, F.; Du, Q.; Zhao, Z.; Nie, K. Web Map-Based POI Visualization for Spatial Decision Support. *Cartogr. Geogr. Inf. Sci.* **2013**, *40*, 172–182. [\[CrossRef\]](#)
61. Liu, K.; Yin, L.; Lu, F.; Mou, N. Visualizing and Exploring POI Configurations of Urban Regions on POI-Type Semantic Space. *Cities* **2020**, *99*, 102610. [\[CrossRef\]](#)
62. Survey, U.S.G. *Landsat Collection 2 Level-2 Science Products*; U.S. Geological Survey: Reston, VA, USA, 2021.
63. Arunachalam, M.; Joshua, R.M.; Kochuparampil, A.J.; Saravanavel, J. ArcOLITIRS: A Toolbox for Radiometric Calibration and Surface Temperature Estimation from Landsat 8 Products in ArcGIS Environment. *J. Indian Soc. Remote Sens.* **2023**, *51*, 453–468. [\[CrossRef\]](#)
64. Wu, T.; Xu, Z.; Chen, R.; Wang, S.; Li, T. Channel Activity Remote Sensing Retrieval Model: A Case Study of the Lower Yellow River. *Remote Sens.* **2023**, *15*, 3636. [\[CrossRef\]](#)
65. Kang, Y.; Chen, Z.; Li, L.; Zhang, Q. Construction of Multidimensional Features to Identify Tea Plantations Using Multisource Remote Sensing Data: A Case Study of Hangzhou City, China. *Ecol. Inform.* **2023**, *77*, 102185. [\[CrossRef\]](#)
66. Chen, D.; Zhang, F.; Zhang, M.; Meng, Q.; Jim, C.Y.; Shi, J.; Tan, M.L.; Ma, X. Landscape and Vegetation Traits of Urban Green Space Can Predict Local Surface Temperature. *Sci. Total Environ.* **2022**, *825*, 154006. [\[CrossRef\]](#) [\[PubMed\]](#)
67. Wang, T.; Chen, S.; Ma, Y.; Chen, Z. Comparison on Scale Effect of Urban Heat Island Defined by Brightness Temperature and Land Surface Temperature. *Geogr. Geo-Inf. Sci.* **2007**, *23*, 73–77. [\[CrossRef\]](#)
68. Liu, Y.; Zhi, W.; Xu, B.; Xu, W.; Wu, W. Detecting High-Temperature Anomalies from Sentinel-2 MSI Images. *ISPRS J. Photogramm. Remote Sens.* **2021**, *177*, 174–193. [\[CrossRef\]](#)
69. Solcerova, A.; van de Ven, F.; van de Giesen, N. Nighttime Cooling of an Urban Pond. *Front. Earth Sci.* **2019**, *7*, 156. [\[CrossRef\]](#)
70. Chavan, G.; Kulkarni, S. Identification of Plant Species Using Remote Sensing Techniques: A Review. *High Technol. Lett.* **2023**, *29*, 267–271.
71. Weng, S.; Yu, S.; Guo, B.; Tang, P.; Liang, D. Non-Destructive Detection of Strawberry Quality Using Multi-Features of Hyperspectral Imaging and Multivariate Methods. *Sensors* **2020**, *20*, 3074. [\[CrossRef\]](#)
72. Weng, S.; Tang, P.; Yuan, H.; Guo, B.; Yu, S.; Huang, L.; Xu, C. Hyperspectral Imaging for Accurate Determination of Rice Variety Using a Deep Learning Network with Multi-Feature Fusion. *Spectrochim. Acta Part A Mol. Biomol. Spectrosc.* **2020**, *234*, 118237. [\[CrossRef\]](#) [\[PubMed\]](#)
73. Campos-Taberner, M.; García-Haro, F.J.; Martínez, B.; Izquierdo-Verdiguier, E.; Atzberger, C.; Camps-Valls, G.; Gilabert, M.A. Understanding Deep Learning in Land Use Classification Based on Sentinel-2 Time Series. *Sci. Rep.* **2020**, *10*, 17188. [\[CrossRef\]](#)
74. Ibrahim, F.; Rasul, G. Urban Land Use Land Cover Changes and Their Effect on Land Surface Temperature: Case Study Using Dohuk City in the Kurdistan Region of Iraq. *Climate* **2017**, *5*, 13. [\[CrossRef\]](#)
75. Chandra, M.A.; Bedi, S.S. Survey on SVM and Their Application in Imageclassification. *Int. J. Inf. Technol.* **2021**, *13*, 1–11. [\[CrossRef\]](#)
76. Zhou, J.; Xiao, M.; Niu, Y.; Ji, G. Rolling Bearing Fault Diagnosis Based on WGWOA-VMD-SVM. *Sensors* **2022**, *22*, 6281. [\[CrossRef\]](#) [\[PubMed\]](#)
77. Aziz, G.; Minallah, N.; Saeed, A.; Frnda, J.; Khan, W. Remote Sensing Based Forest Cover Classification Using Machine Learning. *Sci. Rep.* **2024**, *14*, 69. [\[CrossRef\]](#) [\[PubMed\]](#)
78. Sun, J.; Liu, Y.; Dong, Y.; Xu, B.; Wei, X. Classification of Urban Industrial Heat Sources Based on Suomi-NPP VIIRS Nocturnal Thermal Anomaly Product—A Case Study of Beijing-Tianjin-Hebei Region. *Geogr. Inf. Sci.* **2018**, *34*, 13–19.
79. Cai, S.; Wang, Y.; Zhao, B.; Wang, S.; Chang, X.; Hao, J. The Impact of the “Air Pollution Prevention and Control Action Plan” on PM2.5 Concentrations in Jing-Jin-Ji Region during 2012–2020. *Sci. Total Environ.* **2017**, *580*, 197–209. [\[CrossRef\]](#)

Disclaimer/Publisher’s Note: The statements, opinions and data contained in all publications are solely those of the individual author(s) and contributor(s) and not of MDPI and/or the editor(s). MDPI and/or the editor(s) disclaim responsibility for any injury to people or property resulting from any ideas, methods, instructions or products referred to in the content.